Metal-Organic Frameworks as Playgrounds for Reticulate Single Molecule Magnets

Lucas H. G. Kalinke,[†,‡,#] Danielle Cangussu,[#] Marta Mon,[†] Rosaria Bruno,[§] Estefania Tiburcio,[†] Francesc Lloret,[†] Donatella Armentano[§] Emilio Pardo[†] and Jesus Ferrando Soria*[†]

[†]Departament de Química Inorgànica, Instituto de Ciencia Molecular (ICMOL), Universitat de València, 46980 Paterna, València, Spain

[‡]Instituto Federal de Goiás – IFG, 75131-457, Anápolis, GO, Brazil

#Instituto de Química, Universidade Federal de Goiás, 74690-900, Goiânia, GO, Brazil

[§]Dipartimento di Chimica e Tecnologie Chimiche, Università della Calabria, Rende 87036, Cosenza, Italy

ABSTRACT: Achieving an accurate control on the final structure of Metal-Organic Frameworks (MOFs) is mandatory to obtain target physical properties. Here we describe how the combination of a metalloligand design strategy and a post-synthetic method is a versatile and powerful approach to success on this extremely difficult task. In a first stage, a novel oxamato-based tetranuclear cobalt(III) complex with a tetrahedron-shape geometry is used, for the first time, as metalloligand toward calcium(II) cations to lead a diamagnetic Ca(II)-Co(III) three-dimensional (3D) MOF (**1**). In a second stage, in a single-crystal to single-crystal manner the calcium(II) ions are replaced by terbium (III), dysprosium(III), holmium(III) and erbium(III) ones to yield four isostructural novel Ln(III)-Co(III) [Ln = Tb (**2**), Dy (**3**), Ho (**4**) and Er (**5**)] 3D MOFs. The direct-current (dc) magnetic properties for **2**–**5** reveal behaviors as expected for the ground terms of the magnetic isolated rare-earth ions [$^7F_6$ (Tb^{III}), $^6H_{15/2}$ (Dy^{III}), $^5I_8$ (Ho^{III}) and $^4I_{15/2}$ (Er^{III})]. The analysis of the $\chi_M T$ data indicates that the lowest M_J value is the ground state, that is $M_J = 0$ (**2** and **4**) and $\pm 1/2$ (**3** and **5**). Incipient frequency-dependent alternating current magnetic susceptibility signals are observed for the Kramers' ions (**3** and **5**) under an external applied magnetics field, supporting the presence of slow magnetic relaxation typical of single-molecule magnets.

INTRODUCTION

Metal-Organic Frameworks (MOFs)[1–6] are a class of crystalline porous materials with fascinating high-dimensional structures and interesting chemical and physical properties,[7–12] which have shown applications in such diverse fields as gas separation and adsorption,[13–15] catalysis,[16,17] molecular recognition,[18,19] drug delivery,[20,21] magnetism[22,23] and water remediation.[24,25] The exponential growth of MOFs, to some extent, is related to (*i*) the achieved precise control over the size shape and functionality of MOF's channels[26–28] and (*ii*) their high crystallinity, which offers the possibility to use X-ray crystallography as characterization tool.[29–31] Although a total control of MOF structure it is not always possible to achieve, during the last decade great synthetic efforts have been devoted to implement rational design strategies, underpinned by X-ray crystallography, that allows having control on MOF dimensionality and topology, and consequently on MOF properties.[32–35]

Single-Molecule Magnets (SMMs),[36–43] which also include the so-called Single-Ion Magnets (SIMs), have been traditionally related to paramagnetic high-spin coordination complexes with a high magnetic anisotropy that exhibit slow relaxation of the magnetization –recently, some exciting examples of SMMs have been found for compounds with the lowest M_J value as ground state–, and represent the ultimate limit of miniaturization in the emergent field of Molecular Spintronics.[44–46] The potential applications of magnetic molecules on high-density magnetic memories and quantum information processing have attracted the attention of researchers working in the fields of Molecular Magnetism and Multifunctional Magnetic Materials.[47–51] In fact, through rational molecular-based design strategies, during the last years commendable advances have been achieved on the increase of the temperature to observe magnetic bistability and phase memory time.[52,53] However, there are several daunting challenges that need to be addressed to move toward building molecular-based devices. One of the most complex is the controlled spatial organization of magnetic molecules to build large-scale ordered arrays.

The unique properties of MOFs make them, *a priori*, excellent platforms to take a leap forward toward gaining some insight on this complex issue.[54,55] In fact, seminal investigations exist on the use of MOFs as reticulating agents to organize SMMs.[56–62] The main strategies of these works are either the direct self-assembly of appealing polytopic donor ligands with metal ions[63–66] and the structuration/encapsulation of preformed SMMs.[67–72] Here, on the basis of our previous investigations on the metalloligand design strategy and Post-Synthetic Methodologies (PSMs) to build robust oxamate-based MOFs with interesting physical properties,[73–76] we propose the combined use of both approaches for the controlled organization of lanthanides metal ions into a 3D network. Despite subtle changes on lanthanide coordination geometry could affect, enormously, the magnetic properties of the resulting SIM-MOFs, we consider the first steps of this approach, showed hereafter, could

be highly beneficial for the further development of Molecular Spintronics.

Synthesis and X-ray Crystal Structure. We report herein the combined application of the metalloligand design strategy and PSMs to obtain a novel family of water-stable 3D MOFs of formulae $\{Ca^{II}_6(H_2O)_{24}[Co^{III}_4(tpatox)_4]\} \cdot 44H_2O$ (**1**), $\{[Tb^{III}_6(H_2O)_{24}[Co^{III}_4(tpatox)_4]](NO_3)_6\} \cdot 49H_2O$ (**2**) $\{[Dy^{III}_6(H_2O)_{24}[Co^{III}_4(tpatox)_4]](NO_3)_6\} \cdot 53H_2O$ (**3**), $\{[Ho^{III}_6(H_2O)_{30}[Co^{III}_4(tpatox)_4]](NO_3)_6\} \cdot 44H_2O$ (**4**) and $\{[Er^{III}_6(H_2O)_{24}[Co^{III}_4(tpatox)_4]](NO_3)_6\} \cdot 58H_2O$ (**5**), where tpatox^{6-} is the *N*,*N*',*N*'-tris(4-phenyl)aminetris(oxamate) ligand. Interestingly, the reported post-synthetic metal exchange process is reflected in a change of the magnetic properties of the original precursor (**1**) to afford, as theoretically expected, two novel examples of MOFs of the bimetallic oxamate family exhibiting SIM behavior (**3** and **5**). The direct reactions between $Na_{12}[Co^{III}_4(tpatox)_4] \cdot 6H_2O$ and $Ln(NO_3)_3 \cdot 5H_2O$ result into unsuccessful attempts to obtain by direct synthesis **2**–**5**.

1 was obtained as dark brown cubes by slow diffusion of aqueous solutions of the tetranuclear Co(III) complex $Na_{12}[Co^{III}_4(tpatox)_4] \cdot 6H_2O$ and $CaCl_2$ (2 : 3 molar ratio) in H-shaped tubes at room temperature. Here, it is worth noting that this is the first time that a preformed tetranuclear complex is used as metalloligand to build oxamate-based MOFs –where commonly preformed mono- or dinuclear complexes are used, and lately, one-dimensional rod-like secondary building units.[77–80] **2**–**5** were obtained through a post-synthetic, solid-state, metal exchange process by immersing crystals of **1** in saturated aqueous solutions of $M(NO_3)_3 \cdot 5H_2O$ [M = Tb (**2**), Dy (**3**), Ho (**4**) and Er (**5**)] for two weeks. The whole process was monitored visually and no crystal dissolution was observed. The final crystals shown the same size and shape as the pristine ones.

The crystal structures of **1** and **3**–**5** could be determined by single-crystal X-diffraction (Figures 1-3 and S1-S5). Isostructurality of **2** with **3**–**5** have been confirmed by cell parameters determination (see Table S1 in Supporting Information). **1** and **3**–**5** are isostructural and crystallize in the F*m*(-3) space group of the cubic system with a cell volume of *ca*. 50000 Å^3. Their structures consist of tri-nodal (3,12,2)-connected 3D networks (*vide infra*) of calcium(II)-cobalt(III) in **1** or Ln(III)-cobalt(III) metal ions, [Ln = Dy (**3**), Ho (**4**) and Er (**5**)] featuring $[Co_4(tpatox)_4]^{12-}$ tetrahedral cages (Figure 1a) connected by Ca(II) (**1**) (Figure 1b) or Ln(III) ions (Figure 2), which built highly porous structures with virtual diameters of *ca*. 0.9 nm, where a vastly solvated nanospace contributes to stabilize metal ions environment (Figures 1c, 3 and S1-S4).

Scheme 1. Chemical structures of the tris(4-phenyl)aminetris(oxamate) ligand (a), highlighting the potential coordination sites and the corresponding tetranuclear cobalt(III) complex with a tetrahedron geometry (b).

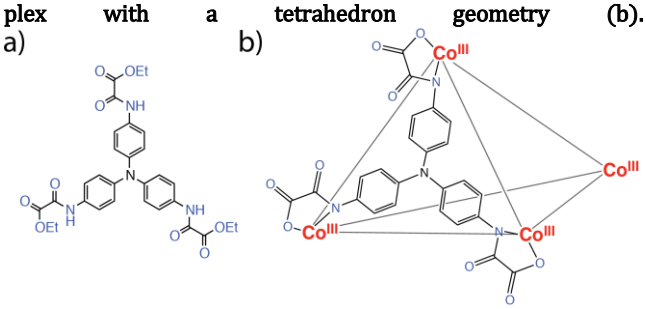

The tripodal tpatox-ligand (Scheme 1 and Figures 1 and S4a) built up highly robust tetrahedral cages being coordinated to Co(III) from oxamate groups. In this way, each Co(III) is chelated by three tpatox-ligand in a distorted octahedral environment with the same Co-O and Co-N bond lengths in **1** with values of 1.934(3) and 1.932(2) Å, respectively. Those values fluctuate in the ranges 1.923(8)-1.963(11) Å and 1.940(12)-1.958(8) Å in **3**–**5**. The Co(III)···Co(III) separation within the cages are of 11.74, 11.69, 11.67 and 11.80 Å for **1** and **3**–**5**, respectively (Figure S4b). Each tetrahedral cage is linked to twelve Ca(II) (**1**) or Ln(III) (**3**–**5**) through oxamate groups of the tpatox ligand (Figures 1b, 2 and S1 and S4b), where Ca(II) or Lanthanides ions act as 2-conneted nodes of the whole net. The Ca(II) and Ln(III)-O distances exhibit averaged values of 2.484(3), 2.44(1), 2.431(9) and 2.42(1) Å, for **1**, **3**–**5**, respectively. Water molecules (not entirely detected from density maps) in **1**, together with nitrate counter ions (in **3**–**5**) complete the coordination environment of each 2-c node (Supporting Information and Figure S5), which exhibit a final eight coordination geometry [or nine for Ho(III)]. A higher coordination number cannot be ruled out because of either the presence of messy peaks on density maps which cannot be modelled for high thermal disorder or thermogravimetric analysis (TGA) (see sections below).

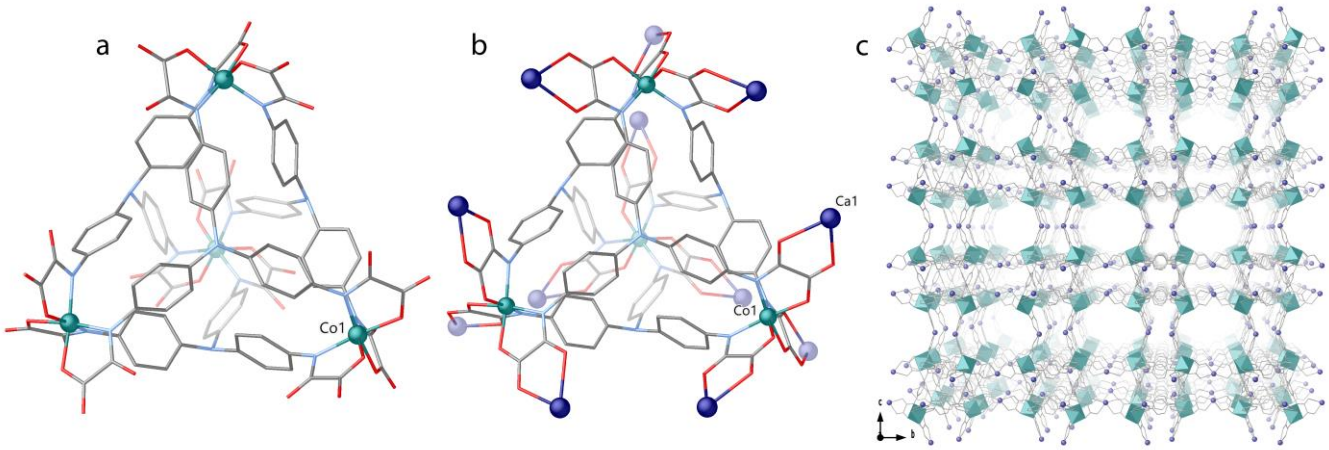

Figure 1. a) Perspective view of $[Co_4(tpatox)_4]^{12-}$ tetrahedral cages of **1** and b) cages connected by twelve Ca(II) metal ions; c) Perspective view along *a* crystallographic axis of porous structure of **1** (the detected crystallization water molecules are omitted for

clarity). Ligands from the network are depicted as gray sticks, cobalt(III) and calcium(III) ions from the network are represented as cyan polyhedral and blue spheres, respectively.

In the geometries around the Dy(III) (**3**), and Er(III) (**5**) the deviation from the ideal eight-coordinate polyhedron, has been evaluated using the program SHAPE (Table S3). The same calculation has been done to evaluate deviation from the ideal nona-coordination around Ho(III) (**4**) (Table S4).[81–83] From the calculation it is evidenced that dysprosium(III) are less distorted than Erbium(III) ions showing biaugmented trigonal-prismatic geometries (C_{2v}) with the estimated deviation parameters of 0.536 and 2.027 for **3** and **5**, respectively. The calculation for Holmium(III) suggests a muffin-like shaped geometry (C_s) around Ho(III) with an estimated deviation from that of 1.845.

A topological analysis of such highly connected framework, by applying the concept of the simplified underlying net,[84] was performed using the computer program TOPOSPRO.[85] It concerns the tripodal tpatox ligands as 3-connected nodes and the $[Co_4(L)_4]$ tetrahedral cages as 6-connected nodes (with twelve links, but each cage is connected through two links to an adjacent cage). Therefore, each triangular tpatox ligand acts as a 3-connected node and connects to three $[Co_4(L)_4]$ tetrahedral cages (Figure 2b, 3 and S4a-b), whereas each $[Co_4(L)_4]$ cage is linked by twelve Ca^{2+} metal ions (or Dy, Ho and Er in **3, 4** and **5,** respectively) to six cages (Figure S4c-d). In this description, the resulting topology is a (3,6)-connected 3D framework. The resulting 3D network can be assigned to an unusual binodal (3,6)-c topology (Figure S4a,d).

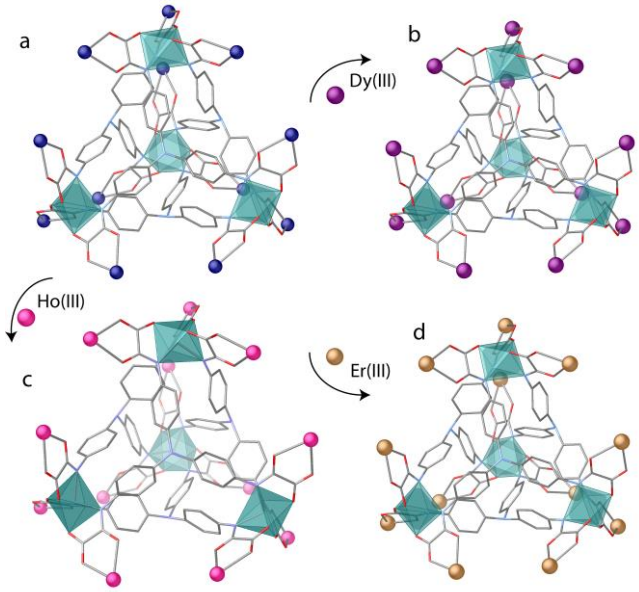

Figure 2. a-d) Perspective view of $[Co_4(tpatox)4]^{12-}$ tetrahedral cages coordinated by twelve 2-c nodes consisting of Ca(II) or Dy(III), Ho(III) and Er(III) post-synthetically exchanged, building isoreticular nets. Ligands from the networks are depicted as gray sticks, cobalt(III), calcium(II), dysprosium(III), holmium(III) and erbium(III) ions are represented as cyan polyhedral and purple, magenta and gold spheres, respectively.

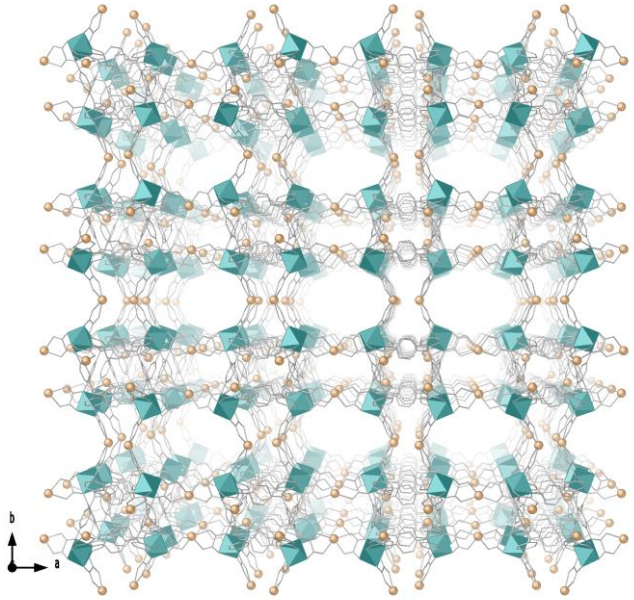

Figure 3. Perspective view along *c* crystallographic axis of porous structure of **5** (the detected crystallization water molecules are omitted for clarity). Ligands from the network are depicted as gray sticks, cobalt(III) and erbium(III) ions from the network are represented as cyan polyhedral and gold spheres, respectively.

Without found solvent molecules, the effective free volumes of **1** and **3–5** are calculated by PLATON analysis to be 70% and 65% of the crystal volume (35373.8 and 31732.4, 31516.2, 31691.3 Å^3 of the 50989 and 48791, 48330, 48940 Å^3 of the unit cell volume for **1** and **3–5**, respectively). In accordance with SCXRD analysis, the channels of **1** and **3–5** are entirely filled by solvent guests (**1**) together with nitrate anions (**3–5**), (Figure S5 and crystallographic details in Supporting Information).

Thermogravimetric Analysis and X-Ray Powder Diffraction. The water content of **1–5** were determined by thermogravimetric analysis (TGA) under a dry N_2 atmosphere. All five compounds show a qualitatively similar behavior, with a fast mass loss from room temperature to *ca.* 473 K, followed by a plateau in the mass loss until decomposition starts. The estimated percentage weight loss values of 33 (**1**), 27 (**2**), 28 (**3**), 27 (**4**) and 29 (**5**) at 473 K (Figure S6 in the Supporting Information), which correspond to 68 (**1**), 73 (**2**), 77 (**3**), 74 (**4**) and 82 (**5**) H_2O molecules. Powder X-ray diffraction (PXRD) studies for **1–5** show a total loss of crystallinity for **1**, when it is removed from water solution. In contrast, **2–5** remain crystalline when exposed to air, but also, they became amorphous with very mild heating. Thus, the PXRD experiments were performed in water suspensions to preclude the partial loss of water molecules and the consequent collapse of the structure in **1–5**. The pureness of the bulk sample, in each compound, was confirmed by the consistency between the experimental PXRD patterns and the theoretical ones extracted from the single crystal X-ray diffraction (Figure 4).

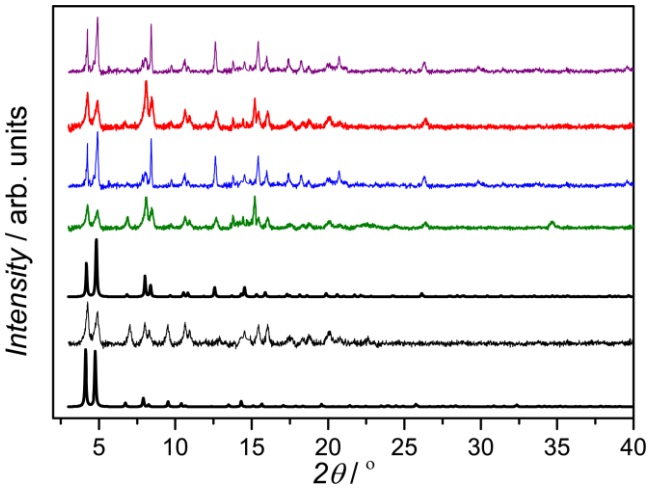

Figure 4. Experimental (solid lines) and calculated (black bold lines) XRPD pattern profiles of the hydrated phases of **1** (black), **2** (green), **3** (blue), **4** (red) and **5** (purple) measured as water suspensions in the 2θ range 2.0–40.0° at room temperature.

Magnetic Properties. The magnetic behavior of **2**–**5**, in the form of the $\chi_M T$ *vs* T plot [χ_M being the molar magnetic susceptibility per mole of Ln(III) ion] are represented in Figures 5–8. At room temperature, the values of $\chi_M T$ are 11.41 (**2**), 13.54 (**3**), 13.18 (**4**) and 10.64 (**5**) $cm^3\ mol^{-1}\ K$. Upon cooling, the $\chi_M T$ values of **2** and **3** practically follow a Curie law until *ca.* 115 K and then start to decrease, meanwhile **4** and **5** steadily decrease from room temperature, to reach values of 7.09 (**2**), 7.43 (**3**), 6.40 (**4**) and 5.21 (**5**) $cm^3\ mol^{-1}\ K$ at 1.9 K. This behavior agrees with the expected one for the ground term of these trivalent rare-earth metal ions, $^7F_6$ (Tb^{III}), $^6H_{15/2}$ (Dy^{III}), $^5I_8$ (Ho^{III}) and $^4I_{15/2}$ (Er^{III}).

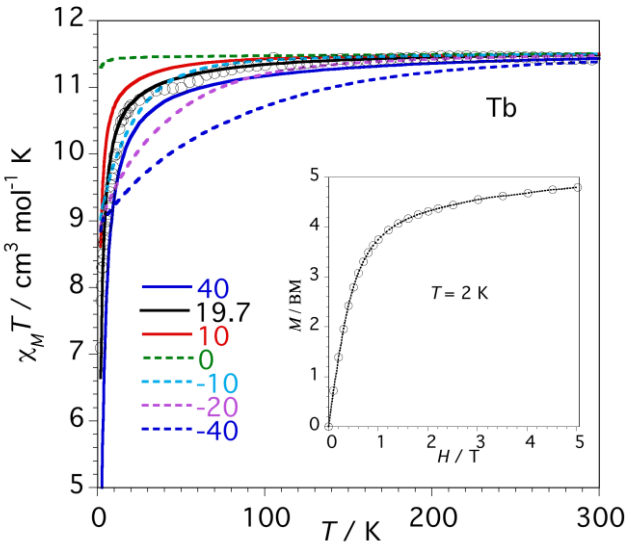

Figure 5. Thermal dependence of the $\chi_M T$ (○) product for **2**. The dashed and solid lines represent the theoretical curves calculated through the Hamiltonian of eq. 1 with the best-fit parameters (see Table 1 and text) as a function of different positive and negative values of Δ expressed in reciprocal centimeters. (inset) Field dependence of M (○) for **2** at T = 2.0 K.

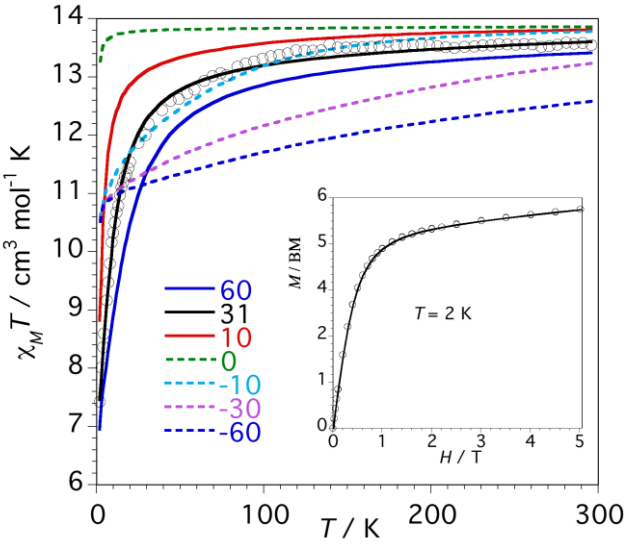

Figure 6. Thermal dependence of the $\chi_M T$ (○) product for **3**. The dashed and solid lines represent the theoretical curves calculated through the Hamiltonian of eq. 1 with the best-fit parameters (see Table 1 and text) as a function of different positive and negative values of Δ expressed in reciprocal centimeters. (inset) Field dependence of M (○) for **3** at T = 2.0 K.

The magnetic properties of **2**–**5** have been analyzed thorough the Hamiltonian of eq. 1, which assumes a ligand-field of axial symmetry for the lanthanide ions,

$$H = \lambda \hat{L}\hat{S} + \Delta\left[\hat{L}_z^2 - \frac{1}{3}L(L+1)\right] + \beta H\left(-\kappa\hat{L} + 2\hat{S}\right) \quad (1)$$

where the first term describes the spin-orbit coupling, the second one accounts for an axial ligand-field component ($x = y \neq z$), and the last one is the Zeeman effect. λ is the spin-orbit coupling parameter, Δ describes the energy gap between the M_L components, and κ is an orbital reduction parameter. The best-fit parameters obtained through the Hamiltonian of eq. 1 by using the *VPMAG* program[86] are listed in Table 1. These parameters provided a quite good match between the experimental and calculated curves, as seen in Figures 5–8. For comparative purposes, it has been also performed several theoretical curves calculated from different Δ values.

Table 1. Best-fit parameters for 2–5

Compound	λ, cm^{-1}	Δ, cm^{-1}	κ
2	-623(4)	19.7(1)	0.987(3)
3	-327(1)	31.3(2)	0.998(3)
4	-699(3)	69.6(3)	0.997(3)
5	-705(8)	61.5(4)	0.989(3)

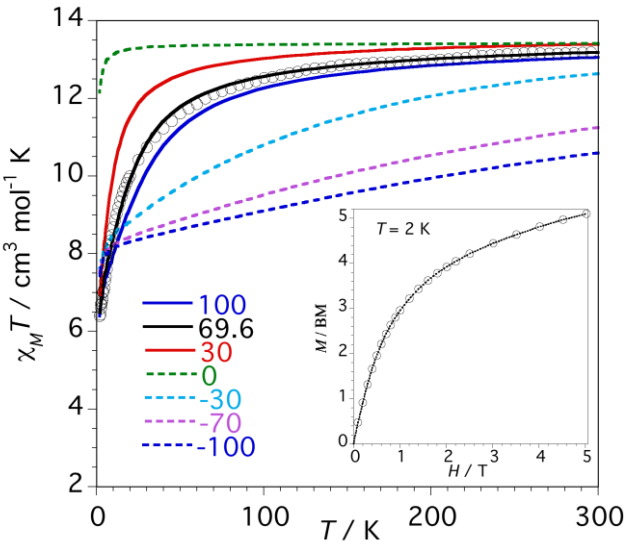

Figure 7. Thermal dependence of the $\chi_M T$ (○) product for **4**. The dashed and solid lines represent the theoretical curves calculated through the Hamiltonian of eq. 1 with the best-fit parameters (see Table 1 and text) as a function of different positive and negative values of Δ expressed in reciprocal centimeters. (inset) Field dependence of M (○) for **4** at T = 2.0 K.

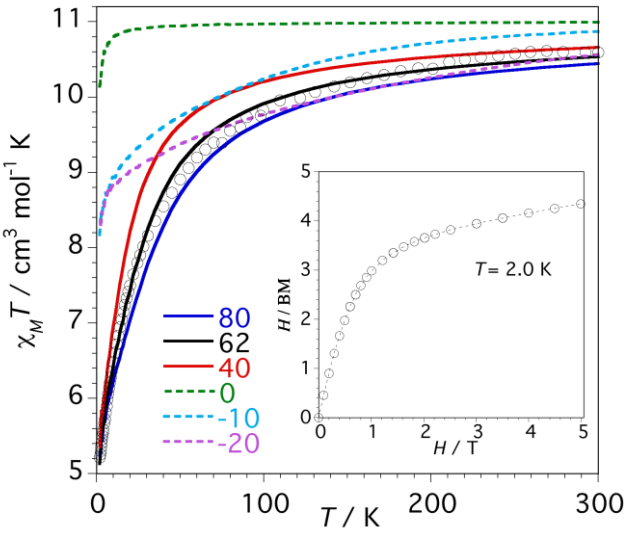

Figure 8. Thermal dependence of the $\chi_M T$ (○) product for **5**. The dashed and solid lines represent the theoretical curves calculated through the Hamiltonian of eq. 1 with the best-fit parameters (see Table 1 and text) as a function of different positive and negative values of Δ expressed in reciprocal centimeters. (inset) Field dependence of M (○) for **5** at T = 2.0 K.

From the analysis of the thermal dependence of the $\chi_M T$ product, the most relevant information we can extract is that the sign of Δ is clearly positive and with a magnitude of a few tens of inverse centimeters for all the studied compounds. As it can be observed from the theoretical curves, negative Δ values would imply a very different shape of $\chi_M T$ curves and a very different magnetic moment for the ground state. $\Delta > 0$ values imply that the lowest M_J value is the ground state, that is M_J = 0 for **2** and **4**, and $M_J = \pm$ ½ for **3** and **5**. The fact that the values of at low temperature are very close to those expected through the Hamiltonian of eq. 1 is indicative of the absence of any important magnetic interaction between the Ln(III) ions, which could strongly influence the spin dynamics (see below). These very weak, if any, magnetic interactions agree with the relatively large metal-metal separation through the possible exchange pathways (across diamagnetic Co^{III} ions) present in this compound.

Interestingly, **3** and **5** exhibit incipient out-of-phase *ac* signals (Figures 9–10), under an applied *dc* magnetic field of 0.1 mT, which is an indicative feature that these compounds could present slow magnetic relaxation of the magnetization below 2.0 K. No out-of-phase signal (χ_M'') of the *ac* magnetic susceptibility was observed for them in absence of an external magnetic field, which it is a common outcome in this type of compounds when a fast quantum tunneling of the magnetization (QTM) is operating. In contrast, **2** and **4** did not show any out-of-phase *ac* signal, with or without the application of an external magnetic field, as expected for a rare-earth metal ion with a $M_J = 0$ as ground state.

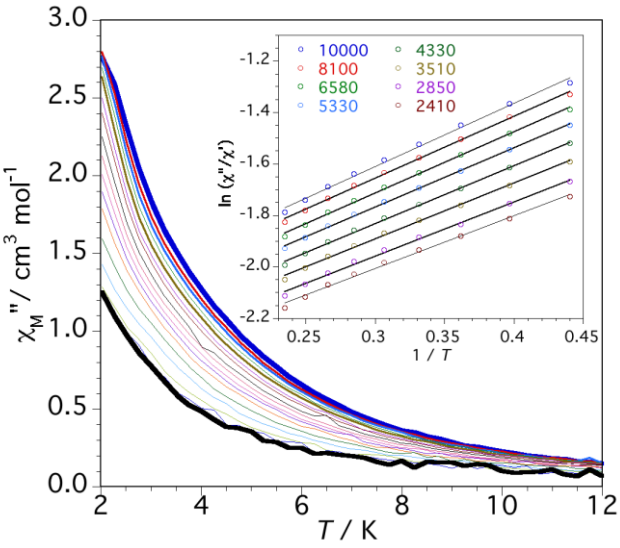

Figure 9. Frequency dependence of the out-of-phase ac susceptibility for **3** under an applied static field of H_{dc} = 1000 G with a ±5.0 G oscillating field at frequencies in the range of 0.075–10 kHz. (Inset) Natural logarithm of the χ_M''/χ_M' ratio vs. $1/T$ at different frequencies.

Indeed, traditionally, it has been associated the presence of magnetic slow relaxation in complexes that combine a strong uniaxial magnetic anisotropy and a ground state with a high-spin value.[87,88] However, **3** and **5**, with the lowest M_J value as ground state, exhibit slow magnetic relaxation under an external *dc* field. Even this could sound counterintuitive, recently, it has been reported slow magnetic relaxation in some Kramers ions with dominant easy-plane magnetic anisotropy –but only under an external magnetic field–, as well as in a series of lanthanides(III) ions with $M_J = \pm 1/2$ as ground state.[89–93] The magnetic behavior of **3** and **5** resembles closely that found in these reported systems.

The absence of maxima in the χ_M'' curves have precluded the analysis of the out-of-phase signals with commonly use methods.[94–96] However, taking the assumption that the SMM relaxation has just one characteristic time –corresponding to a Debye

relaxation process driven by one activation energy (E_a)– the relaxation time (τ) may be written in terms of the Arrhenius law $\tau = \tau_0 \exp(E_a/k_B T)$.[97] Then, taking into account that $\chi_M''/\chi_M' = 2\pi\upsilon\tau$ where υ is the experimental ac field exciting frequency, it is possible to roughly evaluate the values of E_a and τ_0 through the expression $\ln(\chi_M''/\chi_M') = \ln(\pi\upsilon\tau) + E_a/k_B T$. The values obtained for E_a and τ_0 were 3.24(4) (**3**) and 9.90(7) (**5**) cm^{-1} and 3.2(2) x 10^{-6} (**3**) and 1.5(2) x 10^{-7} (**5**) s, respectively, which are similar to the ones of other SMMs previously analyzed through this method (inset Figures 9 and 10).[98,99]

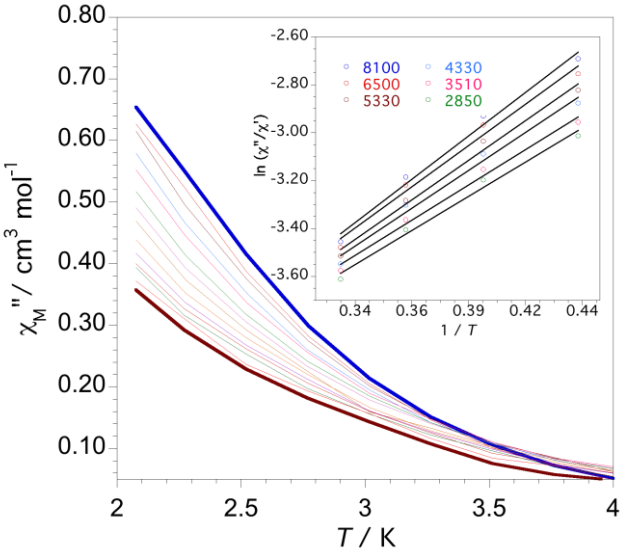

Figure 10. Frequency dependence of the out-of-phase ac susceptibility for **5** under an applied static field of H_{dc} = 1000 G with a ±5.0 G oscillating field at frequencies in the range of 5–10 kHz. (Inset) Natural logarithm of the χ_M''/χ_M' ratio vs. $1/T$ at different frequencies.

Conclusions

We report the combined use of the metalloligand design strategy and post-synthetic methodologies for the controlled organization of lanthanides metal ions into a 3D network. In a first stage, we use a preformed novel oxamato-based tetranuclear cobalt(III) complex with a tetrahedron-shape geometry as metalloligand toward calcium(II) cations to lead the diamagnetic Ca(II)-Co(III) 3D MOF **1**. Then, in a single-crystal to single-crystal process, calcium(II) ions are replaced by terbium (III), dysprosium(III), holmium(III) and erbium(III) ones to yield a family of four isostructural novel Ln(III)-Co(III) [Ln = Tb (**2**), Dy (**3**), Ho (**4**) and Er (**5**)] 3D MOFs. Interestingly, the MOFs with Kramers' ions (**3** and **5**) show incipient frequency-dependent alternating current magnetic susceptibility signals under an external applied magnetics field, which –after a carefull analysis– support the presence of slow magnetic relaxation typical of single-molecule magnets. Overall, this work presents a two-fold relevance: (*i*) the use, for the first time, of a preformed oxamato-based tetranuclear complex with tetrahedron geometry as metalloligand, and (ii) a step forward toward the controlled organization of magnetic molecules to build large-scale ordered arrays.

EXPERIMENTAL SECTION

Preparation of $\{Ca^{II}_6(H_2O)_{24}[Co^{III}_4(tpatox)_4]\} \cdot 44H_2O$ (1). A multigram scale synthesis of **1** was carried out by direct reaction of water solutions of $Na_{12}\{Co_4(tpatox)_4\} \cdot 6H_2O$ and $CaCl_2$: a 15 mL portion of the $CaCl_2$ solution (0.66 g, 6 mmol) was added dropwise over 20 mL of another solution containing $Na_{12}\{Co_4(tpatox)_4\} \cdot 6H_2O$ (2.62 g, 1 mmol). The mixture was stirred at r.t. for 24 h. The resulting dark brown polycrystalline powder was filtered off, gently washed with water and air-dried. Yield: 3.15 g, 85 %; Anal.: calcd for $C_{96}H_{184}Ca_6Co_4N_{16}O_{104}$ (3702.7): C, 31.14; H, 5.01; N, 6.05%. Found: C, 31.11; H, 5.04; N, 6.09%; IR (KBr): ν = 1602 cm^{-1} (C=O).

X-ray quality dark brown cubic prisms of **1** could be obtained by slow diffusion of aqueous solutions containing stoichiometric amounts of $Na_{12}\{Co_4(tpatox)_4\} \cdot 6H_2O$ (0.262 g, 0.1 mmol) and $CaCl_2$ (0.066 g, 0.6 mmol) in a H-shaped tube standing at 18 °C after several weeks.

Preparation of $\{[Ln^{III}_6(H_2O)_m[Co^{III}_4(tpatox)_4]](NO_3)_6\} \cdot nH_2O$ [**2**: Ln = Tb, m = 24, n = 49; **3**: Ln = Dy, m = 24, n = 53; **4**: Ln = Ho, m = 30, n = 44; **5**: Ln = Er, m = 24, n = 58]: Well-formed dark brown cubic prisms of **2**–**5**, suitable for X-ray diffraction, were obtained by immersing crystals of **1** for 2 weeks in saturated aqueous solutions of $Ln(NO_3)_3 \cdot 5H_2O$ [Ln = Tb (**2**), Dy (**3**), Ho (**4**) and Er (**5**)]. **2**: Yield: 94%; Anal.: calcd (%) for $C_{96}H_{194}Co_4N_{22}O_{127}Tb_6$ (4877.9): C, 23.64; H, 4.01; N, 6.32. Found: C, 23.67; H, 4.06; N, 6.41; IR (KBr): ν = 1604 cm^{-1} (C=O). **3**: Yield: 92%; Anal.: calcd (%) for $C_{96}H_{202}Co_4Dy_6N_{22}O_{131}$ (4971.4): C, 23.19; H, 4.10; N, 6.20. Found: C, 23.17; H, 4.15; N, 6.31; IR (KBr): ν = 1605 cm^{-1} (C=O). **4**: Yield: 94%; Anal.: calcd (%) for $C_{96}H_{196}Co_4Ho_6N_{22}O_{128}$ (4932.1): C, 23.38; H, 4.01; N, 6.25. Found: C, 23.48; H, 4.05; N, 6.21; IR (KBr): ν = 1603 cm^{-1} (C=O). **5**: Yield: 93%; Anal.: calcd (%) for $C_{96}H_{212}Co_4Er_6N_{22}O_{136}$ (5090.1): C, 22.65; H, 4.20; N, 6.06. Found: C, 22.60; H, 4.17; N, 6.01; IR (KBr): ν = 1604 cm^{-1} (C=O).

Single-Crystal X-ray Diffraction. Diffraction data for **1** and **3**–**5** were collected on a Bruker-Nonius X8APEXII CCD area detector diffractometer using graphite-monochromated Mo-Kα radiation (λ = 0.71073 Å). Crystal data for **1**–**5**: cubic, space group *Fm*(-3), T = 90(2) K, Z = 8.

1: $C_{96}H_{184}Ca_6Co_4N_{16}O_{104}$, a = 37.082(3) Å, V = 50989(13) $Å^3$; **3**: $C_{96}H_{202}Co_4Dy_6N_{22}O_{131}$, a = 36.541(8) Å, V = 48791(31) $Å^3$; **4**: $C_{96}H_{196}Co_4Ho_6N_{22}O_{128}$, a = 36.426(6) Å, V = 48330(24) $Å^3$; **5**: $C_{96}H_{212}Co_4Er_6N_{22}O_{136}$, a = 36.578(11) Å, V = 48940(44) $Å^3$. Further details can be found in the Supplementary Information.

CCDC 1938635, 1938636–1938638 for **1, 3–5**, respectively contain the supplementary crystallographic data for this paper.

X-ray Powder Diffraction. Polycrystalline sample of **1**–**5** was introduced into 0.5 mm borosilicate capillary prior to being mounted and aligned on a Empyrean PANalytical powder diffractometer, using Cu Kα radiation (λ = 1.54056 Å). Five repeated measurements were collected at room temperature (2θ = 2–40°) and merged in a single diffractogram.

Thermogravimetric analysis. The TGA measurements were performed on a crystalline sample of **1**–**5** under a dry N_2 atmosphere with a Mettler Toledo TGA/STDA 851^e thermobalance operating at a heating rate of 10 ºC min^{-1}.

Magnetic Measurements. Variable-temperature (2.0–300 K) direct current (*dc*) magnetic susceptibility measurements under an applied field of 100 G (T < 30K) and 5.0 kG (T > 30 K), and variable-field (0–5.0 T) magnetization measurements at 2.0 K were carried out for **2**–**5** with a Quantum Design MPMS-XL7 SQUID magnetometer.

Variable-temperature (2.0–12 K) alternating current (*ac*) magnetic susceptibility measurements under ± 5.0 G oscillating field at frequencies in the range of 1–10.0 kHz were carried

out for **2**–**5** under an applied static field of 1.0 kG with a Quantum Design Physical Property Measurement System (PPMS). Static *dc* magnetic measurements were carried out for **2**–**5** by powdering and restraining the sample in order to prevent any displacement due to its magnetic anisotropy, whereas the dynamic *ac* magnetic measurements were carried out by using frozen aqueous solutions of polycrystalline samples of **2**–**5**. The susceptibility data were corrected for the diamagnetism of the constituent atoms and the sample holder.

ASSOCIATED CONTENT

Supporting Information

Additional preparations and physical characterization data. Additional Figures (Figures S1-S8). Crystallographic details and refinement for **1**–**5** (Table S1). CCDC 1938635-1938638. This material is available free of charge via the Internet at http://pubs.acs.org.

AUTHOR INFORMATION

Corresponding Author

To whom correspondence should be addressed: jesus.ferrando@uv.es.

Notes

The authors declare no competing financial interests.

ACKNOWLEDGMENT

This work was supported by the MINECO (Spain) (Projects CTQ2016-75671-P, CTQ2016-75068-P and Excellence Unit "Maria de Maeztu" MDM-2015-0538) and the Ministero dell'Istruzione, dell'Università e della Ricerca (Italy). L. H. G. K. thanks CAPES "Coordenação de Aperfeiçoamento de Pessoal de Nível Superior" for grants. E.P. acknowledges the financial support of the European Research Council under the European Union's Horizon 2020 research and innovation programme / ERC Grant Agreement No 814804, MOF-reactors. Thanks, are also extended to the "Fondo per il finanziamento delle attività base di ricerca" (D.A.). J. F.-S. acknowledges financial support from the "Subprograma Atracció de Talent-Contractes Postdoctorals de la Universitat de Valencia" and "Juan de la Cierva-Incorporación-2017" program.

REFERENCES

(1) Furukawa, H.; Cordova, K. E.; O'Keeffe, M.; Yaghi, O. M. The chemistry and applications of metal-organic frameworks. *Science* **2013**, *341*, 974.

(2) Eddaoudi, M.; Sava, D. F.; Eubank, J. F.; Adil, K.; Guillerm, V. Zeolite-like metal-organic frameworks (ZMOFs): design, synthesis and properties. *Chem. Soc. Rev.* **2015**, *44*, 228–249.

(3) Cui, Y.; Li, B.; He, H.; Zhou, W.; Chen, B.; Qian, G. Metal-Organic Frameworks as Platforms for Functional Materials. *Acc. Chem. Res.* **2016**, *49*, 483–493.

(4) Islamoglu, T.; Goswami, S.; Li, Z.; Howarth, A. J.; Farha, O. K.; Hupp, J. T. Postsynthetic Tuning of Metal-Organic Frameworks for Targeted Applications. *Acc. Chem. Res.* **2017,** *50*, 805–813.

(5) Maurin, G.; Serre, C.; Cooper, A.; Férey, G. The new age of MOFs and of their porous-related solids. *Chem. Soc. Rev.* **2017**, *46*, 3104–3107.

(6) Yuan, S.; Feng, L.; Wang, K.; Pang, J.; Bosch, M.; Lollar, C.; Sun, Y.; Qin, J.; Yang, X.; Zhang, P.; Wang, Q.; Zou, L.; Zhang, Y.; Zhang, L.; Fang, Y.; Li, J.; Zhou, H.-C. Stable Metal-Organic Frameworks: Design, Synthesis and Applications. *Adv. Mater.* **2018**, *30*, 1704303.

(7) Li, P.; Vermeulen, N. A.; Malliakas, C. D.; Gómez-Gualdrón, D. A.; Howarth, A. J.; Mehdi, B. L.; Dohnalkova, A.; Browning, N. D.; O'Keeffe, M.; Farha, O. K. Bottom-up construction of a superstructure in a porous uranium-organic crystal. *Science* **2017,** *356*, 624–627.

(8) Kim, H.; Yang, S.; Rao, S. R.; Narayanan, S.; Kapustin, E. A.; Furukawa, H.; Umans, A. S.; Yaghi, O. M. Water harvesting from air with metal-organic frameworks powered by natural sunlight. *Science* **2017**, *356*, 430–434.

(9) Reed, D. A.; Keitz, B. K.; Oktawiec, J.; Mason, J. A.; Runčevski, T.; Xiao, D. J.; Darago, L. E.; Crocellà, V.; Bordiga, S.; Long, J. R. A spin transition mechanism for cooperative adsorption in metal-organic frameworks. *Nature* **2017**, *550*, 96–100.

(10) Shen, K.; Zhang, L.; Chen, X.; Liu, L.; Zhang, D.; Han, Y.; Chen, J.; Long, J.; Luque, R.; Li, Y.; Chen, B. Ordered macro-microporous metal-organic framework single crystals. *Science* **2018**, *359*, 206–210.

(11) Shen, K.; Zhang, L.; Chen, X.; Liu, L.; Zhang, D.; Han, Y.; Chen, J.; Long, J.; Luque, R.; Li, Y.; Chen, B. Ordered macro-microporous metal-organic framework single crystals. *Science* **2018**, *359*, 206–210.

(12) Qin, J.-S..; Yuan, S.; Zhang, L.; Li, B.; Du, D.-Y.; Huang, N.; Guan, W.; Drake, H. F.; Pang, J.; Lan, Y.-Q.; Alsalme, A.; Zhou, H.-C. Creating Well-Defined Hexabenzocoronene in Zirconium Metal-Organic Framework by Postsynthetic Annulation. *J. Am. Chem Soc.* **2019**, *141*, 2054–2060.

(13) Cadiau, A.; Adil, K.; Bhatt, P. H.; Belmabkhout, Y.; Eddaoudi, M. A metal-organic framework-based splitter for separating propylene from propane. *Science* **2016**, *353*, 137–140.

(14) Li, H.; Wang, K.; Sun, Y.; Lollar, C.; Li, J.; Zhou, H.-C. Recent advances in gas storage and separation using metal-organic frameworks. *Mater. Today* **2018**, *21*, 108–121.

(15) Belmabkhout, Y.; Bhatt, P. M.; Adil, K.; Pillai, R. S.; Cadiau, A.; Shkurenko, A.; Maurin, G.; Liu, G.; Koros, W. J.; Eddaoudi, M. Natural gas upgrading using a fluorinated MOF with tuned H_2S and CO_2 adsorption selectivity. *Nat. Energy* **2018**, *3*, 1059–1066.

(16) Zhang, X.; Huang, Z.; Ferrandon, M.; Yang, D.; Robison, L.; Li, P.; C Wang, T. C.; Delferro, M.; Farha, O. K. Catalytic Chemoselective Functionalization of Methane in a Metal-Organic Framework. *Nat. Catal.* **2018,** *1,* 356–362.

(17) Mon, M.; Rivero-Crespo, M. A.; Ferrando-Soria, J.; Vidal-Moya, A.; Boronat, M.; Leyva-Pérez, A.; Corma, A.; Hernandez-Garrido, J. C.; López-Haro, M.; Calvino, J. J.; Ragazzon, G.; Credi, A.; Armentano, D.; Pardo, E. Synthesis of Densely Pack-

aged, Ultrasmall Pt^0_2 Clusters within a Thioether-Functionalized MOF: Catalytic Activity in Industrial Reactions at Low Temperature. *Angew. Chem., Int. Ed.* **2018**, *57*, 6186–6191.

(18) Navarro-Sánchez, J.; Argente-García, A. I.; Moliner-Martínez, Y.; Roca-Sanjuán, D.; Antypov, D.; Campíns-Falcó, P.; Rosseinsky, M. J.; Martí-Gastaldo, C. Peptide Metal-Organic Frameworks for Enantioselective Separation of Chiral Drugs. *J. Am. Chem. Soc.* **2017**, *139*, 4294–4297.

(19) Martell, J. D.; Porter-Zasada, L. B.; Forse, A. C.; Siegelman, R. L.; Gonzalez, M. I.; Oktawiec, J.; Runčevski, T.; Xu, J.; Srebro-Hooper, M.; Milner, P. J.; Colwell, K. A.; Autschbach, J.; Reimer, J. A.; Long, J. R. Enantioselective Recognition of Ammonium Carbamates in a Chiral Metal-Organic Framework. *J. Am. Chem. Soc.* **2017**, *139*, 16000–16012.

(20) Simon-Yarza, T.; Giménez-Marqués, M.; Mrimi, R.; Mielcarek, A.; Gref, R.; Horcajda, P. Serre, C.; Couvreur, P. A Smart Metal-Organic Framework Nanomaterial for Lung Targeting. *Angew. Chem. Int. Ed.* **2017**, *56*, 15565–15569.

(21) Dong, Z.; Sun, Y.; Chu, J.; Zhang, X.; Deng, H. Multivariate Metal-Organic Frameworks for Dialing-in the Binding and Programming the Release of Drug Molecules. *J. Am. Chem. Soc.* **2017**, *139*, 14209–14216.

(22) Li, W.; Sun, L.; Jarillo-Herrero, P.; Dincă, M.; Li, J. High temperature ferromagnetism in π-conjugated two-dimensional metal-organic frameworks. *Chem. Sci.* **2017**, *8*, 2859–2867.

(23) Pedersen, K. S.; Perlepe, P.; Aubrey, M. L.; Woodruff, D. N.; Reyes-Lillo, S. E.; Reinholdt, A.; Voigt, L.; Li, Z.; Borup, K.; Rouzières, M.; Samohvalov, D.; Wilhelm, F.; Rogalev, A.; Neaton, J. B.; Long J. R.; Clérac, R. Formation of the layered conductive magnet $CrCl_2(pyrazine)_2$ through redox-active coordination chemistry. *Nat. Chem.* **2018**, *10*, 1056–1061.

(24) Kobielska, P. A.; Howarth, A. J.; Farha, O. K.; Nayak, S. Metal-organic frameworks for heavy metal removal from water. *Coord. Chem. Rev.* **2018**, *358*, 92–107.

(25) Mon, M.; Bruno, R.; Ferrando-Soria, J.; Armentano, D.; Pardo, E. Metal-organic framework technologies for water remediation: towards a sustainable ecosystem. *J. Mater. Chem. A* **2018**, 6, 4912–4947.

(26) Pang, J.; Yuan, S.; Qin, J.; Wu, M.; Lollar, C. T.; Li, J.; Huang, N.; Li, B.; Zhang, P.; Zhou, H.-C. Enhancing Pore-Environment Complexity Using a Trapezoidal Linker: Toward Stepwise Assembly of Multivariate Quinary Metal-Organic Frameworks. *J. Am. Chem. Soc.* **2018**, *140*, 12328–12332.

(27) Guillerm, V.; Grancha, T.; Imaz, I.; Juanhuix, J.; Maspoch, D. Zigzag ligands for Transversal Design in Reticular Chemistry: Unveiling New Structural Opportunities for Metal-Organic Frameworks. *J. Am. Chem. Soc.* **2018**, *140*, 10153–10157.

(28) Jiang, H.; Jia, J.; Shkurenko, A.; Chen, Z.; Adil, K.; Belmabkhout, Y.; Weselinski, L. J.; Assen, A. H.; Xue, D.-X. O'Keeffe, M.; Eddaoudi, M. Enriching the reticular chenistry repertorie: merged nets approach for the rational design of intricate mixed-linker MOF platforms. *J. Am. Chem Soc.* **2018**, *140*, 8858–8867.

(29) Inokuma, Y.; Yoshioka, S.; Ariyoshi, J.; Arai, T.; Hitora, Y.; Takada, K.; Matsunaga, S.; Rissanen, K.; Fujita, M. X-ray analysis on the nanogram to microgram scale using porous complexes. *Nature* **2013**, *495*, 461–466.

(30) Bloch, W. M.; Champness, N. R.; Doonan, C. J. X-ray Crystallography in Open-Framework Materials. *Angew. Chem., Int. Ed.* **2015**, *54*, 12860–12867.

(31) Mon, M.; Bruno, R.; Ferrando-Soria, J.; Bartella, L.; Di Donna, L.; Talia, M.; Lappano, R.; Maggiolini, M.; Armentano, D.; Pardo, E. Crystallographic snapshots of host-guest interactions in drugs@metal-organic frameworks: towards mimicking molecular recognition processes. *Mater. Horizons* **2018**, *5*, 683–690.

(32) Guillerm, V.; Kim, D.; Eubank, J. F.; Luebke, R.; Liu, X.; Adil, K.; Lah, M. S.; Eddaoudi, M. A supermolecular building approach for the design and construction of metal-organic frameworks. *Chem. Soc. Rev.* **2014**, *43*, 6141–6172.

(33) Schoedel, A.; Li, M.; Li, D.; O'Keeffe, M.; Yaghi, O. M. Structures of Metal-Organic Frameworks with Rod Secondary Building Units. *Chem. Rev.* **2016**, *116*, 12466–12535.

(34) Cohen, S. M. The Postsynthetic Renaissance in Porous Solids. *J. Am. Chem. Soc.* **2017**, *139*, 2855–2863.

(35) Kirchon, A.; Feng, L.; Drake, H. F.; Joseph, E. A.; Zhou, H.-C. From fundamentals to applications: a toolbox for robust and multifunctional MOF materials. *Chem. Soc. Rev.* **2018**, *47*, 8611–8638.

(36) Gastteschi, D.; Sessoli, R.; Villain, J. *Molecular Nanomaterials* (Oxford University Press, Oxford, 2006).

(37) Woodruff, D. N.; Winpenny, R. E. P.; Layfield, R. A. Lanthanide Single-Molecule Magnets *Chem. Rev.* **2013**, *113*, 5110–5148.

(38) Demir, S.; Jeon, I.-R.; Long, J. R.; Harris, T. D. Radical ligand-containing single-molecule magnets. *Coord. Chem. Rev.* **2015**, *289*, 149–176.

(39) Liu, J.; Chen, Y.-C.; Liu, J.-L.; Vieru, V.; Ungur, L.; Jia, J.-H.; Chibotaru, L. F.; Lan, Y.; Wernsdorfer, W.; Gao, S.; Chen, X.-M.; Tong, M.-L. A stable pentagonal bipyramidal Dy(III) single-ion magnet with a record magnetization reversal barrier over 1000 K. *J. Am. Chem. Soc.* **2016**, *138*, 5441−5450.

(40) Ferrando-Soria, J.; Vallejo, J.; Castellano, M.; Martínez-Lillo, J.; Pardo, E.; Cano, J.; Castro, I.; Lloret, F.; Ruiz-García, R.; Julve, M. Molecular Magnetism, Quo Vadis? A Historical Perspective from a Coordination Chemist Viewpoint☆. *Coord. Chem. Rev.* **2017**, *339*, 17−103.

(41) Natterer, F. D.; Yang, K.; Paul, W.; Willke, P.; Choi, T.; Greber,T.; Heinrich, A. J.; Lutz, C. P. Reading and writing single-atommagnets. *Nature* **2017**, *543*, 226−228.

(42) Ding, Y.-S.; Yu, K.-X.; Reta, D.; Ortu, F.; Winpenny, R. E. P.; Zheng, Y.-Z.; Chilton, N. F. Field- and temperature-dependent quantum tunnelling of the magnetisation in a large barrier single-molecule magnet. *Nat. Commun.* **2018**, *9*, 3134−3143.

(43) Bunting, P. C.; Atanasov, M.; Damgaard-Møller, E.; Perfetti, M.; Crassee, I.; Orlita, M.; Overgaard, J.; van Slageren, J.; Neese, F.; Long, J. R. A linear cobalt(II) complex with maximal orbital angular momentum from a non-Aufbau ground state. *Science* **2018**, *362*.

(44) Bogani, L.; Wernsdorfer, W. Molecular spintronics using single-molecule magnets. *Nat. Mater.* **2008**, *7*, 179−186.

(45) Sanvito, S. Molecular spintronics. *Chem. Soc. Rev.* **2011**, *40*, 3336−3355.

(46) Cornia, A.; Seneor, P. The molecular way. *Nat. Mater.* **2017**, *16*, 505−506.

(47) Tiele, S.; Balestro, F.; Ballou, R.; Klyatskaya, S.; Ruben, M.; Wernsdorfer, W. Electrically driven nuclear spin resonance in single-molecule magnets. *Science* **2014**, *344*, 1135–1138.

(48) Shiddiq, M.; Komijami, D.; Duan, Y.; Gaita-Ariño, A.; Coronado, E.; Hill, S. Enhancing coherence in molecular spin qubits via atomic clock transitions. *Nature* **2016**, *531*, 348–351.

(49) Ferrando-Soria, J.; Magee, S. A.; Chiesa, A.; Carretta, S.; Santini, P.; Vitorica-Yrezabal, I. J.; Tuna, F.; Whitehead, G. F. S.; Sproules, S.; Lancaster, K. M.; Barra, A.-L.; Timco, G. A.; McInnes, E. J. L.; Winpenny, R. E. P. Switchable Interaction in Molecular Double Qubits. *Chem* **2016**, *1*, 727−752.

(50) Malavolti, L.; Briganti, M.; Hänze, M.; Serrano, G.; Cimatti, I.; McMurtrie, G.; otero, E.; Ohresser, P.; Totti, F.; Mannini, M.; Sessoli, R.; Loth, S. Tunable Spin-Superconductor Coupling of spin 1/2 Vanadyl Phthalocyanine Molecules. *Nano Lett.* **2018**, *18*, 7955–7961.

(51) Morita, T.; Damjanović, M.; Katoh, K.; Kitagawa, Y.; Yasuda, N.; Lan, Y.; Wernsdorfer, W.; Breedlove, B. K.; Enders, M.; Yamashita, M. Comparison of the Magnetic Anisotropy and Spin Relaxation Phenomenon of Dinuclear Terbium(III) Phthalocyaninato Single Molecule Magnets Using the Geometric Spin Arrangement. *J. Am. Chem. Soc.* **2018**, *140*, 2995−3007.

(52) Goodwin, C. A. P.; Ortu, F.; Reta, D.; Chilton, N. F.; Mills, D. P. Molecular magnetic hysteresis at 60 K in dysprosocenium. *Nature* **2017**, *548*, 439−442.

(53) Guo, F.-S.; Day, B. M.; Chen, Y.-C.; Tong, M.-L.; Mansikkamäki, A.; Layfield, R. A. Magnetic hysteresis up to 80 K in a dysprosium metallocene single-molecule magnet. *Science* **2018**, *362*, 1400.

(54) Graham, M. J.; Zadrozny, J. M.; Fataftah, M. S.; Freedman, D. E. Forging Solid-State Qubit Design Principles in a Molecular Furnace. *Chem. Mater.* **2017**, *29*, 1885–1897.

(55) Mínguez Espallargas, G.; Coronado, E. Magnetic functionalities in MOFs: from the framework to the pore. *Chem. Soc. Rev.* **2018**, *47*, 533–557.

(56) Kurmoo, M. Magnetic metal-organic frameworks. *Chem. Soc. Rev.* **2019**, *38*, 1353–1379.

(57) Dechambenoit, P.; Long, J. R. Microporous magnets. *Chem. Soc. Rev.* **2011**, *40*, 3249–3265.

(58) Weng, D.-F.; Wang, Z.-M.; Gao, S. Framework-structured weak ferromagnets. *Chem. Soc. Rev.* **2011**, *40*, 3157–3181.

(59) Coronado, E.; Mínguez Espallargas, G. Dynamic magnetic MOFs. *Chem. Soc. Rev.* **2013**, *42*, 1525–1539.

(60) Roy, S.; Chakraborty, A.; Maji, T. K. Lanthanide-organic frameworks for gas storage and as magneto-luminescent materials. *Coord. Chem. Rev.* ***2014****, 273, 139–164*.

(61) *Lanthanide Metal-Organic Frameworks*; Cheng, P., Ed.; Springer-Verlag; Berlin; 2015.

(62) Liu, K.; Zhang, X.; Meng, X.; Shi, W.; Cheng, P.; Powell, A. K. Constraining the coordination geometries of lanthanides centers and magnetic building blocks in frameworks: a new strategy for molecular nanomagnets. *Chem. Soc. Rev.* **2016**, *45*, 2423–2439.

(63) Baldoví, J. J.; Coronado, E.; Gaita-Ariño, A.; Gamer, C.; Giménez-Marqués, M.; Mínguez Espallargas, G. A SIM-MOF: Three-Dimensional Organisation of Single-Ion Magnets with Anion-Exchange Capabilities. *Chem. Eur. J.* **2014**, *20*, 10695–10702.

(64) Zhang, X.; Vieru, V.; Feng, X.; Liu, J.-L.; Zhang, Z.; Na, B.; Shi, W.; Wang, B.-W.; Powell, A. K.; Chibotaru, L. F.; Gao, S.; Cheng, P.; Long, J. R. Influence of Guest Exchange on the Magnetization Dynamics of Dilanthanide Single-Molecule-Magnet Nodes within a Metal-Organic Framework. *Angew. Chem. Int. Ed.* **2015**, *54*, 9861–9865.

(65) Vallejo, J.; Pardo, E.; Viciano-Chumillas, M.; Castro, I.; Amorós, P.; Déniz, M., Ruiz-Pérez, C.; Yuste-Vivas, C.; Krzystek, J.; Julve, M.; Lloret, F.; Cano, J. Reversible solvatomagnetic switching in a single-ion magnet from an entatic state. *Chem. Sci.* **2017**, *8*, 3694–3702.

(66) Huang, G.; Fernandez-Garcia, G.; Badiane, I.; Camarra, M.; Freslon, S.; Guillou, O.; Daiguebonne, C.; Totti, F.; Cador, O.; Guizouarn, T.; Le Guennic, B.; Bernot, K. Magnetic Slow Relaxation in a Metal-Organic Framework Made of Chains of Ferromagnetically Coupled Single-Molecule Magnets. *Chem. Eur. J.* **2018**, *24*, 6983–6991.

(67) Rigamonti, L.; Cotton, C.; Nava, A.; Lang, H.; Rüffer, T.; Perfetti, M.; Sorace, L.; Barra, A.-L.; Lan, Y.; Wernsdorfer, W.; Sessoli, R.; Cornia, A. Diamondoid Structure in a Metal-Organic Framework of Fe_4 Single-Molecule Magnets. *Chem. Eur. J.* **2016**, *22*, 13705–13714.

(68) Aulakh, D.; Pyser, J. B.; Zhang, X.; Yakovenko, A. A.; Dunbar, K. R.; Wriedt, M. Metal−organic frameworks as platforms for the controlled nanostructuring of single-molecule magnets. J. Am. Chem. Soc. **2015**, *137*, 9254−9257.

(69) Zadrozny, J. M.; Gallagher, A. T.; Harris, T. D.; Freedman, D. E. A Porous Array of Clock Qubits *J. Am. Chem. Soc.* **2017**, *139*, 7089–7094.

(70) Yamabayashi, T.; Atzori, M.; Tesi, L.; Cosquer, G.; Santanni, F.; Boulon, M.; Morra, E.; Benci, S.; Torre, R.; Chiesa, M.; Sorace, L.; Sessoli, R. Yamashita, M. Scaling up Electronic Spin Qubits into a Three-Dimensional Metal-Organic Framework. *J. Am. Chem. Soc.* **2018**, *140*, 12090–12101.

(71) Yu, C.-J.; Krzyaniak, M. D.; Fataftah, M. S.; Wasielewski, M. R.; Freedman, D. E. A concentrated array of copper porphyrin candidate qubits *Chem. Sci.* **2019**, *10*, 1702–1708.

(72) Aulakh, D.; Liu, L.; Varghese, J. R.; Xie, H.; Islamoglu, T.; Duell, K.; Kung, C.-W.; Hsiung, C.-E.; Zhang, Y.; Drout, R. J.; Farha, O. K.; Dunbar, K. R.; Han, Y.; Wriedt, M. Direct Imaging of Isolated Single-Molecule Magnets in Metal-Organic Frameworks. *J. Am. Chem. Soc.* **2019**, DOI: 10.1021/jacs.8b11374.

(73) Grancha, T.; Ferrando-Soria, J.; Zhou, H.-C.; Gascon, J.; Seoane, B.; Pasán, J.; Fabelo, O.; Julve, M.; Pardo, E. Postsynthetic Improvement of the Physical Properties in a Metal-Organic Framework through a Single Crystal to Single Crystal Transmetallation. *Angew. Chem., Int. Ed.* **2015**, *54*, 6521–6525.

(74) Fortea-Pérez, F. R.; Mon, M.; Ferrando-Soria, J.; Boronat, M.; Leyva-Pérez, A.; Corma, A.; Herrera, J. M.; Osadchii, D.; Gascon, J.; Armentano, D.; Pardo, E. The MOF-driven synthesis of supported palladium clusters with catalytic activity for carbene-mediated chemistry. *Nat. Mater.* **2017**, *16*, 760–766.

(75) Mon, M.; Tiburcio, E.; Ferrando-Soria, J.; Gil San Millán, R.; Navarro, J. A. R.; Armentano, D.; Pardo, E. A post-synthetic approach triggers selective and reversible sulphur dioxide adsorption on a metal-organic framework. *Chem. Commun.* **2018**, *54*, 9063–9066.

(76) Tejeda-Serrano, M.; Mon, M.; Ross, B.; Gonell, F.; Ferrando-Soria, J.; Leyva-Pérez, A.; Armentano, D.; Pardo, E. Isolated Fe(III)–O Catalyze the Hydrogenation of Acetlyne in Ethylene Flows under Front-End Industrial Conditions. *J. Am. Chem. Soc.* **2018**, *140*, 8827–8832.

(77) Ferrando-Soria, J.; Pasán, J.; Ruiz-Pérez, C.; Journaux, Y.; Julve, M.; Lloret, F.; Pardo, E. Spin Control in Oxamato-Based Manganese(II)-Copper(II) Coordination Polymers with Brick-Wall Layer Architectures. *Inorg. Chem.* **2011**, *50*, 8694–8696.

(78) Ferrando-Soria, J.; Grancha, T.; Julve, M.; Cano, J.; Lloret, F.; Journaux, Y.; Pasán, J.; Ruiz-Pérez, C.; Pardo, E. Ligand effects on the dimensionality of oxamato-bridged mixed-metal open-framework magnets. *Chem. Commun.* **2012**, *48*, 3539–3541.

(79) Grancha, T.; Mon, M.; Lloret, F.; Ferrando-Soria, J.; Journaux, Y.; Pasán, J.; Pardo, E. Double Interpenetration in a Chiral Three-Dimensional Magnet with a (10,3)-a Structure. *Inorg. Chem.* **2015**, *54*, 8890–8892.

(80) Grancha, T.; Qu, X.; Julve, M.; Ferrando-Soria, J.; Armentano, D.; Pardo, E. Rational Synthesis of Chiral Metal-Organic Frameworks from Preformed Rodlike Secondary Building Units. *Inorg. Chem.* **2017**, *56*, 6551–6557.

(81) Zabrodsky, H.; Peleg, S.; Avnir, D. Continuous symmetry measures. *J. Am. Chem. Soc.* **1992**, *114*, 7843–7851.

(82) Pinsky, M.; Avnir, D. Continuous Symmetry Measures. 5. The Classical Polyhedra. *Inorg. Chem.* **1998**, *37*, 5575–5582.

(83) Llunell, M.; Casanova, D.; Cirera, J.; Alemany, P.; Alvarez, S. SHAPE 2.1, Program for Calculating Continuous Shape Measures of Polyhedral Structures; Universitat de Barcelona: Spain, **2013**.

(84) Bonneau, C.; O'Keeffe, M.; Proserpio, D. M.; Blatov, V. A.; Batten, S. R.; Bourne, S. A.; Lah, M. S.; Eon, J.-G.; Hyde, S. T.; Wigging, S. B.; Öhrström, L. Deconstruction of Crystalline Networks into Underlying Nets: Relevance for Terminology Guidelines and Crystallographic Databases. *Cryst. Growth Des.* **2018**, *18*, 3411−3418.

(85) Blatov, V. A.; Shevchenko, A. P.; Proserpio, D. M. Applied Topological Analysis of Crystal Structures with the Program Package ToposPro. *Cryst. Growth Des.* **2014**, *14*, 3576−3586.

(86) Cano, J. VPMAG, Revison 03; University of Valencia: Spain, **2004**.

(87) Sessoli, R.; Gatteschi, D.; Caneschi, A.; Novak, M. Magnetic bistability in a metal-ion cluster. *Nature* **1993**, *365*, 141−143.

(88) Villain, J.; Hartman-Boutron, F.; Sessoli, R.; Rettori, A. Magnetic Relaxation in Big Magnetic Molecules. *Europhys. Lett.* **1994**, 27, 159−164.

(89) Zadrozny, J. M.; Atanasov, M.; Bryan, A. M.; Lin, Ch-Y.; Rekken, B. D.; Power, P. P.; Neese, F.; Long, J. R. Slow magnetization dynamics in a series of two-coordinate iron(II) complexes. *Chem. Sci.* **2013**, *4*, 125−138.

(90) Colacio, E.; Ruiz, J.; Ruiz, E.; Cremades, E.; Krzystek, J.; Carretta, S.; Cano, J.; Guidi, T.; Wernsdorfer, W.; Brechin, E. K. Slow Magnetic Relaxation in a CoII−YIII Single-Ion Magnet with Positive Axial Zero-Field Splitting. *Angew. Chem., Int. Ed.* **2013**, *52*, 9130−9134.

(91) Gómez-Coca, S.; Urtizberea, A.; Cremades, E.; Alonso, P. J.; Camon, A.; Ruiz, E.; Luis, F. Origin of slow magnetic relaxation in Kramers ions with non-uniaxial anisotropy. *Nat. Commun.* **2014**, *5*, 1−8.

(92) Marinho, M. V.; Reis, D. O.; Oliveira, w. X. C.; Marques, L. F.; Stumpf, H. O.; Déniz, M.; Pasán, J.; Ruiz-Pérez, C.; Cano, J.; Lloret, F.; Julve, M. Photoluminescent and Slow Magnetic Relaxation Studies on Lanthanides(III)-2,5-pyrazinedicarboxylate Frameworks. *Inorg. Chem.* **2017**, *56*, 2108−2123.

(93) Alexandru, M.-G.; Visinescu, D.; Shova, S.; Lloret, F.; Julve, M. Cyanido-Bridged $\{Ln^{III}W^{V}\}$ Heterobinuclear Complexes: Synthesis and Magneto-Structural Study. *Inorg. Chem.* **2017**, *56*, 12594−12605.

(94) Cole, K. S.; Cole, R. H. Dispersion and Absorption in Dielectrics I. Alternating Current Characteristics *J. Chem. Phys.* **1941**, *9*, 341−352.

(95) Orbach, R. Spin-Lattice Relaxation in Rare-Earth Salts. *Proc. R. Soc. London, Ser. A* **1961**, A*264*, 458−484.

(96) Van Vleck, H. Paramagnetic Relaxation Times for Titanium and Chrome Alum. *Phys. Rev.* **1940**, 57, 426.

(97) Dinca, A. S.; Vallejo, J.; Shova, S.; Lloret, F.; Julve, M.; Andruh, M. Synthesis, crystal structure and magnetic properties of a new $[Zn^{II}_6Dy^{III}_6]$ dodecanuclear motif. *Polyhedron* **2013**, *65*, 238−243.

(98) Bartolomé, J.; Filoti, G.; Kuncser, V.; Schinteie, G.; Mereacre, V.; Anson, C. E.; Powell, A. K.; Prodius, D.; Turta, C. Magnetostructural correlations in the tetranuclear series of $\{Fe_3LnO_2\}$ butterfly core clusters: Magnetic and Mössbauer spectroscopic study. *Phys. Rev. B* **2009**, *80*, 014430.

(99) Ferrando-Soria, J.; Cangussu, D.; Eslava, M.; Journaux, Y.; Lescouëzec, R.; Julve, M.; Lloret, F.; Pasán, J.; Ruix-Pérez, C.; Lloret, F.; Paulsen, C.; Pardo, E. Rational Enantioselective Design of Chiral Heterobimetallic Single-Chain Magnets: synthesis, Crystal Structures and Magnetic Properties of Oxamato-Bridged $M^{II}Cu^{II}$ Chains (M = Mn, Co). *Chem. Eur. J.* **2011**, 17, 12482–12494.

We report the combined use of the metalloligand design strategy and post-synthetic methodologies to build-up a family of isostructural MOFs as playgrounds toward the controlled spatial organization of single-molecule magnets.

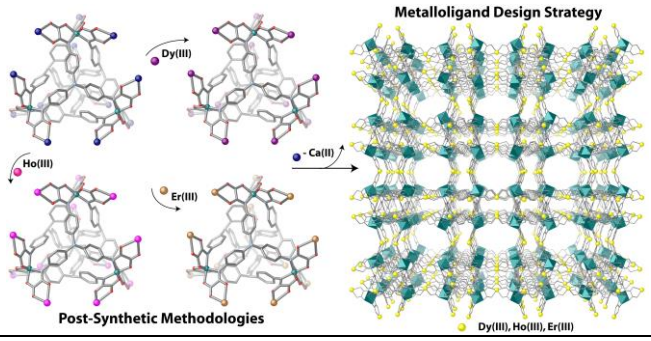

Supporting Information (SI) for the manuscript:

Metal-Organic Frameworks as Playgrounds for Reticulate Single Molecule Magnets

Lucas H. G. Kalinke,[†,‡,#] Danielle Cangussu,[#] Marta Mon,[†] Rosaria Bruno,[§] Estefania Tiburcio,[†] Francesc Lloret,[†] Donatella Armentano,[§] Emilio Pardo[†] and Jesús Ferrando-Soria*[†]

[†]*L. H. G. Kalinke, M. Mon, E. Tiburcio, Prof. Francesc Lloret, Dr. E. Pardo, Dr. J. Ferrando-Soria*
Departamento de Química Inorgánica, Instituto de Ciencia Molecular (ICMOL). Universitat de València
Catedrático Jose Beltrán Martínez, 2.
46980, Paterna (Valencia), Spain.
E-mail: jesus.ferrando@uv.es

[‡]*L. H. G. Kalinke.*
Instituto Federal de Goiás–IFG, 75131-457, Anápolis (Goiás), Brazil.

[#]*L. H. G. Kalinke, Prof. D. Cangussu.*
Instituto de Química, Universidade Federal de Goiás, 74690-900, Goiâna, GO, Brazil.

[§]*R. Bruno, Prof. D. Armentano.*
Dipartimento di Chimica e Tecnologie Chimiche. Università della Calabria. Via Pietro Bucci, 12c.
87030, Rende (Cosenza), Italy.

Experimental Section

Materials. All chemicals were of reagent grade quality. They were purchased from commercial sources and used as received. The synthesis of tris(4-nitrophenyl)amine and tris(4-aminophenyl)amine were prepared according literature procedure.[1]

H_3Et_3-(tpatox) [*N*,*N*',*N*''-tris(4-phenyl)aminetris(oxamate)]: tris(4-aminophenyl)amine (4.35 g, 15.0 mmol) was dissolved in 200 mL of tetrahydrofuran under N_2 atmosphere and charged with triethylamine (6.25 mL, 45.0 mmol). To the resulting reaction mixture, another solution containing ethyl chlorooxacetate (5.0 mL, 45.0 mmol) in tetrahydrofuran (25 mL) was added dropwise under vigorous stirring at 0 °C on an ice-bath to give a yellow suspension. The reaction mixture was heated to reflux for 4 h. After cooling, the small amount of white solid (Et_3NHCl) formed was filtered off and the resulting yellow solution was then concentrated in a rotatory evaporator to afford an orange oil that solidified when water (50 mL) was added. After 1 h of stirring, the yellow solid obtained was filtered off, washed with a small amount of diethyl ether and dried under vacuum. Yield: 8.15 g, 92%; Anal. calcd (%) for $C_{30}H_{30}N_4O_9$ (590.6): C 61.01, H 5.12, N 9.48; found: C 61.11, H 5.23, N 9.52; ^{1}H NMR ($CDCl_3$): 1.36 (t, 9H; $3CH_3$), 4.35 (q, 6H; $3CH_2$), 6.99 (d, 6H; 6CH), 7.46 (d, 6H; 6CH), 8.78 (s, 3H; 3NH); IR (KBr): ν = 3292 (N-H), 3120 and 3052 cm^{-1} (C-H), 1750, 1705 and 1690 cm^{-1} (C=O).

$Na_{12}\{Co_4(tpatox)_4\} \cdot 6H_2O$: A water suspension (50 mL) of H_3Et_3-(tpatox) (2.96 g, 5 mmol) was treated with aqueous NaOH (1.2 g, 30 mmol; 25 mL). The suspension was maintained under vigorous stirring and heating to 50 ºC until complete solubilization of the ligand. Another aqueous solution (25 mL) of $Co(NO_3)_2 \cdot 6H_2O$ (1.46 g, 5 mmol) was then added dropwise while the reaction mixture was stirred. The resulting deep brown solution was concentrated to a volume of 50 mL in a rotary evaporator. The mixture was then allowed to stand at 0 °C on an ice-bath for 30 minutes, and finally it was filtered to remove solid particles. The solvent of the resulting deep brown solution was removed in a rotatory evaporator to afford a brown polycrystalline solid that was gently washed with acetone filtered off and dried under vacuum. Yield: 2.79 g, 85%; Anal.: calcd (%) for $C_{96}H_{60}Co_4N_{16}Na_{12}O_{42}$ (2621.20): C, 43.99; H, 2.31; N, 8.55. Found: C, 44.01; H, 2.28; N, 8.51; IR (KBr): ν = 3438 cm^{-1} (O-H), 3038 cm^{-1} (C-H), 1644 and 1620 cm^{-1} (C=O).

$\{Ca^{II}_6(H_2O)_{24}[Co^{III}_4(tpatox)_4]\} \cdot 44H_2O$ (1): A multigram scale synthesis of **1** was carried out by direct reaction of water solutions of $Na_{12}\{Co_4(tpatox)_4\} \cdot 6H_2O$ and $CaCl_2$: a 15 mL portion of the $CaCl_2$ solution (0.66 g, 6 mmol) was added dropwise over 20 mL of another solution containing $Na_{12}\{Co_4(tpatox)_4\} \cdot 6H_2O$ (2.62 g, 1 mmol). The mixture was stirred at r.t. for 24 h. The resulting dark brown polycrystalline powder was filtered off, gently washed with water and air-dried. Yield: 3.15 g, 85 %; Anal.: calcd for $C_{96}H_{184}Ca_6Co_4N_{16}O_{104}$ (3702.7): C, 31.14; H, 5.01; N, 6.05%. Found: C, 31.11; H, 5.04; N, 6.09%; IR (KBr): ν = 1602 cm^{-1} (C=O).

X-ray quality dark brown cubic prisms of **1** could be obtained by slow diffusion of aqueous solutions containing stoichiometric amounts of $Na_{12}\{Co_4(tpatox)_4\} \cdot 6H_2O$ (0.262 g, 0.1 mmol) and $CaCl_2$ (0.066 g, 0.6 mmol) in a H-shaped tube standing at 18 °C after several weeks.

$\{[Ln^{III}_6(H_2O)_m[Co^{III}_4(tpatox)_4]](NO_3)_6\} \cdot nH_2O$ [2: Ln = Tb, m = 24, n = 49; 3: Ln = Dy, m = 24, n = 53; 4: Ln = Ho, m = 30, n = 44; 5: Ln = Er, m = 24, n = 58]: Well-formed dark brown cubic prisms of **2**–**5**, suitable for X-ray diffraction, were obtained by immersing crystals of **1** for 2 weeks in saturated aqueous solutions of $Ln(NO_3)_3 \cdot 5H_2O$ [Ln = Tb (**2**), Dy (**3**), Ho (**4**) and Er (**5**)]. **2**: Yield: 94%; Anal.: calcd (%) for $C_{96}H_{194}Co_4N_{22}O_{127}Tb_6$ (4877.9): C, 23.64; H, 4.01; N, 6.32. Found: C, 23.67; H, 4.06; N, 6.41; IR (KBr): ν = 1604 cm^{-1} (C=O). **3**: Yield: 92%; Anal.: calcd (%) for $C_{96}H_{202}Co_4Dy_6N_{22}O_{131}$ (4971.4): C, 23.19; H, 4.10; N, 6.20. Found: C, 23.17; H, 4.15; N, 6.31; IR (KBr): ν = 1605 cm^{-1} (C=O). **4**: Yield: 94%; Anal.: calcd (%) for $C_{96}H_{196}Co_4Ho_6N_{22}O_{128}$ (4932.1): C, 23.38; H, 4.01; N, 6.25. Found: C, 23.48; H, 4.05; N, 6.21; IR (KBr): ν = 1603 cm^{-1} (C=O). **5**: Yield: 93%; Anal.: calcd (%) for $C_{96}H_{212}Co_4Er_6N_{22}O_{136}$ (5090.1): C, 22.65; H, 4.20; N, 6.06. Found: C, 22.60; H, 4.17; N, 6.01; IR (KBr): ν = 1604 cm^{-1} (C=O).

Physical Techniques. Elemental (C, H, N) and ICP-MS analyses were performed at the Microanalytical Service of the Universitat de València. ^{1}H NMR spectra were recorded at room temperature on a Bruker AC 200 (200.1 MHz) spectrometer. FT–IR spectra were recorded on a Perkin-Elmer 882 spectrophotometer as KBr pellets. The thermogravimetric analysis was performed on crystalline samples under a dry N_2 atmosphere with a Mettler Toledo TGA/STDA 851 thermobalance operating at a heating rate of 10 ºC min^{-1}. Scanning Electron Microscopy coupled with Energy Dispersive X–

ray (SEM/EDX) was carried out with a XL 30 ESEM (PHILIPS) microscope equipped with a home-made EDAX energy dispersive X-ray detector.

X-ray crystallographic data collection and structure refinement. Crystals of **1**, and **2-5** were selected and mounted on a MITIGEN holder in Paratone oil and very quickly placed on a liquid nitrogen stream cooled at 90 K to avoid the possible degradation upon dehydration. Diffraction data were collected on a Bruker-Nonius X8APEXII CCD area detector diffractometer using graphite-monochromated Mo-K_α radiation (λ = 0.71073 Å). Unfortunately, the poor quality of crystals of **2** precluded any possibility for data acquisition, anyway it was possible to extract cell parameters confirming isostructurality with the whole family (Table S1). The data were processed through SAINT[2] reduction and SADABS[3] multi-scan absorption software. The structures were solved with the SHELXS structure solution program, using the Patterson method. The model was refined with version 2018/3 of SHELXL against F^2 on all data by full-matrix least squares.[4]

Bearing in mind that, crystals of **2**–**5**, suitable for X-ray diffraction, were obtained by immersing crystals of **1** for 2 weeks in saturated aqueous solutions of $Ln(NO_3)_3 \cdot 5H_2O$ [Ln = Tb (**2**), Dy (**3**), Ho (**4**) and Er (**5**)], after a crystal-to-crystal transformation it is reasonable to observe a quite poor diffraction power of the samples even if in present of heavy atoms. However, the solution and refinement parameters are suitable, compared with MOFs structures generally reported, thus we are convinced that the structures found are consistent.

In all samples, all non-hydrogen atoms were refined anisotropically with restraints applied on displacement parameters applied in some case on ligand fragments in **3** (SIMU and DELU) and on defined water molecules (ISOR). In samples **3**, **4** and **5** the high maxima of density detected are due to absorption and can be considered as ripples of Ln(III). The solvent water molecules were highly disordered and only in few amount (respect to overall amount identified by TGA) detected from density maps and modelled. Moreover, NO_3^- counter-anions could not be found from ΔF map. The quite large channels featured by this series of MOFs likely account for that. The contribution to the diffraction pattern from the highly disordered solvent molecules (352, 424, 352 and 464 molecules in **1**, **3**–**5**, respectively) and undetected NO_3^- anions (48 anions for **3**–**5**) located in the voids (that amount to 70% in **1** and 65% of the unit cell in **3**–**5**, respectively) was subtracted from the observed data through the SQUEEZE method, implemented in

PLATON.[5] Taking into account the further diffuse electron density related to coordinated water molecules exhibiting a large dynamical disorder, these values are in good agreement with recovered number of electrons (appended in CIFs) and TGA analysis (Figure S6).

The hydrogen atoms of the ligand, were set in calculated positions and refined as riding atoms, whereas they were neither found nor calculated on defined water molecules.

A summary of the crystallographic data and structure refinement for compounds is given in Table S1. The comments for the alerts A and B are described in the CIFs using the validation reply form (vrf). CCDC reference numbers are 1938635 and 1938636–1938638 for **1** and **3**–**5**, respectively.

The final geometrical calculations on free voids and the graphical manipulations were carried out with PLATON implemented in WinGX,[6] and CRYSTAL MAKER programs,[7] respectively.

X-ray Powder Diffraction Measurements. The corresponding polycrystalline samples of **1**–**5** were introduced into 0.5 mm borosilicate capillaries prior to being mounted and aligned on an Empyrean PANalytical powder diffractometer, using Cu Kα radiation (λ = 1.54056 Å). For each sample, three repeated measurements were collected at room temperature (2θ = 2–40°) and merged in a single diffractogram. The spinning option was disabled due to the presence of water solvent within the capillaries, which accounts for the slight asymmetry observed in some of the peaks. The collected data were analyzed with the X'Pert HighScore Plus software.

Magnetic Measurements. Variable-temperature (2.0–300 K) direct current (*dc*) magnetic susceptibility measurements under an applied field of 100 G (T < 30K) and 5.0 kG (T > 30 K), and variable-field (0–5.0 T) magnetization measurements at 2.0 K were carried out for **2**–**5** with a Quantum Design MPMS-XL7 SQUID magnetometer. Variable-temperature (2.0–12 K) alternating current (*ac*) magnetic susceptibility measurements under ± 5.0 G oscillating field at frequencies in the range of 1–10.0 kHz were carried out for **2**–**5** under an applied static field of 1.0 kG with a Quantum Design Physical Property Measurement System (PPMS). Static *dc* magnetic measurements were carried out for **2**–**5** by powdering and restraining the sample in order to prevent any

displacement due to its magnetic anisotropy, whereas the dynamic *ac* magnetic measurements were carried out by using frozen aqueous solutions of polycrystalline samples of **2**–**5**. The susceptibility data were corrected for the diamagnetism of the constituent atoms and the sample holder.

Table S1. Summary of Crystallographic Data for **1**–**5**.

Compound	**1**	**2**[c]	**3**	**4**	**5**
Formula	$C_{96}H_{184}Ca_6Co_4N_{16}O_{104}$		$C_{96}H_{202}Co_4Dy_6N_{22}O_{131}$	$C_{96}H_{196}Co_4Ho_6N_{22}O_{128}$	$C_{96}H_{212}Co_4Er_6N_{22}O_{136}$
M (g mol^{-1})	3702.78		4971.50	4932.04	5090.14
λ (Å)	0.71073	0.71073	0.71073	0.71073	0.71073
Crystal system	Cubic	Cubic	Cubic	Cubic	Cubic
Space group	*Fm*(-3)	*Fm*(-3)	*Fm*(-3)	*Fm*(-3)	*Fm*(-3)
a (Å)	37.082(3)	36.52(1)	36.541(8)	36.426(6)	36.578(11)
V (Å^3)	50989(13)	48707(60)	48791(31)	48330(24)	48940(44)
Z	8	8	8	8	8
ρ_{calc} (g cm^{-3})	0.965		1.354	1.356	1.382
μ (mm^{-1})	0.450		2.170	2.298	2.392
T (K)	90	90	90	90	90
θ range for data collection (°)	0.951 - 24.995		0.965 - 26.357	0.968 - 26.419	0.964 - 26.000
Completeness to θ = 25.0	100%		100%	100%	100%
Measured reflections	105390		175933	77472	69831
Unique reflections (Rint)	3956 (0.14)		4369 (0.10)	4360 (0.12)	4223
Observed reflections [$I > 2\sigma(I)$]	2570		3173	3746	2853
Goof	1.070		1.711	1.158	1.824
R^a [$I > 2\sigma(I)$] (all data)	0.0642 (0.1221)		0.1817 (0.2029)	0.1310 (0.1411)	0.1566 (0.1956)
wR^b [$I > 2\sigma(I)$] (all data)	0.1743 (0.1978)		0.4762 (0.4992)	0.3881 (0.3810)	0.4840 (0.4977)

[a] $R = \sum(|F_o| - |F_c|)/\sum|F_o|$. [b] $wR = [\sum w(|F_o| - |F_c|)^2/\sum w|F_o|^2]^{1/2}$. [c] The poor quality of the crystals of **2** allowed only cell parameters determination.

Table S2. Selected data from the ICP–MS[a] and SEM/EDX[b].

		Compound 2		
Metal	*% mass*[a]	*Metal stoichiometry*[a]	*% mass*[b]	*Metal stoichiometry*[b]
Co	4.833	4.00	4.80	3.97
Tb	19.646	6.03	19.48	5.98
		Compound 3		
Metal	*% mass*[a]	*Metal stoichiometry*[a]	*% mass*[b]	*Metal stoichiometry*[b]
Co	4.73	3.99	4.71	3.97
Dy	19.644	6.01	19.78	6.05
		Compound 4		
Metal	*% mass*[a]	*Metal stoichiometry*[a]	*% mass*[b]	*Metal stoichiometry*[b]
Co	4.644	4.00	4.62	3.98
Ho	19.527	6.01	19.75	6.08
		Compound 5		
Metal	*% mass*[a]	*Metal stoichiometry*[a]	*% mass*[b]	*Metal stoichiometry*[b]
Co	4.789	4.02	4.86	4.08
Er	20.390	6.03	20.46	6.05

[a]Solid samples were digested with 0.5 mL of HNO_3 69% at 60°C for 4 hours followed by the addition of 0.5 mL of HCl 37% and digestion 80°C for 1 hour. [b]Scanning Electron Microscopy-Energy Dispersive X-ray spectroscopy. Solid samples were mounted on an electrically conductive carbon tape to perform the ananlysis.

Table S3. Possible geometries of eight- coordinated metal centers and deviation parameters calculated by SHAPE from ideal polyhedron in **3** and **5**.

	IDEAL GEOMETRY	SYMMETRY	**3**	**5**
OP-8	Octagon	D_{8h}	26.195	32.310
HPY-8	Heptagonal pyramid	C_{7v}	23.078	24.334
HBPY-8	Hexagonal bipyramid	D_{6h}	17.936	16.509
CU-8	Cube	O_h	13.275	12.341
SAPR-8	Square antiprism	D_{4d}	2.194	2.700
TDD-8	Triangular dodecahedron	D_{2d}	2.563	2.259
JGBF-8	Johnson - Gyrobifastigium (J26)	D_{2d}	13.908	13.906
JETBPY-8	Johnson - Elongated triangular bipyramid (J14)	D_{3h}	27.158	28.374
JBTPR-8	Johnson - Biaugmented trigonal prism (J50)	C_{2v}	1.280	**2.027**
BTPR-8	Biaugmented trigonal prism	C_{2v}	**0.536**	13.293
JSD-8	Snub disphenoid (J84)	D_{2d}	3.824	4.302
TT-8	Triakis tetrahedron	T_d	13.770	13.087
JGBF-8	Elongated trigonal bipyramid	D_{3h}	13.908	13.906

Table S4. Possible geometries of nona- coordinated metal centers and deviation parameters calculated by SHAPE from ideal polyhedron in **4**.

	IDEAL GEOMETRY	SYMMETRY	**4**
EP-9	Enneagon	D_{9h}	30.269
OPY-9	Octagonal pyramid	C_{8v}	20.080
HBPY-9	Heptagonal bipyramid	D_{7h}	17.500
JTC-9	Triangular cupola (J3) = trivacant cuboctahedron	C_{3v}	13.467
JCCU-9	Capped cube (Elongated square pyramid, J8)	C_{4v}	10.969
CCU-9	Capped cube	C_{4v}	9.786
JCSAPR-9	Capped sq. antiprism (Gyroelongated square pyramid J10)	C_{4v}	4.398
CSAPR-9	Capped square antiprism	C_{4v}	2.891
JTCTPR-9	Tricapped trigonal prism (J51)	D_{3h}	6.387
TCTPR-9	Tricapped trigonal prism	D_{3h}	3.783
JTDIC-9	Tridiminished icosahedron (J63)	C_{3v}	13.389
HH-9	Hula-hoop	C_{2v}	9.309
MFF-9	Muffin	C_s	**1.845**

Table S5. Selected *ac* magnetic data under an applied static field of 1000 G[a] for **2** and **3**.

Compound	τ_0[b] / s	E_a[b] / cm^{-1}
3	3.2 x 10^{-6}	3.24
5	1.5 x 10^{-7}	9.90

[a]Applied *dc* magnetic field. [b]Values of the preexponential factor (τ_0) and activation energy (E_a) are calculated through the equation: $\ln(\chi_M''/\chi_M') = \ln(\omega\tau_0) + E_a/k_BT$ (see text and Figures 9 and 10).

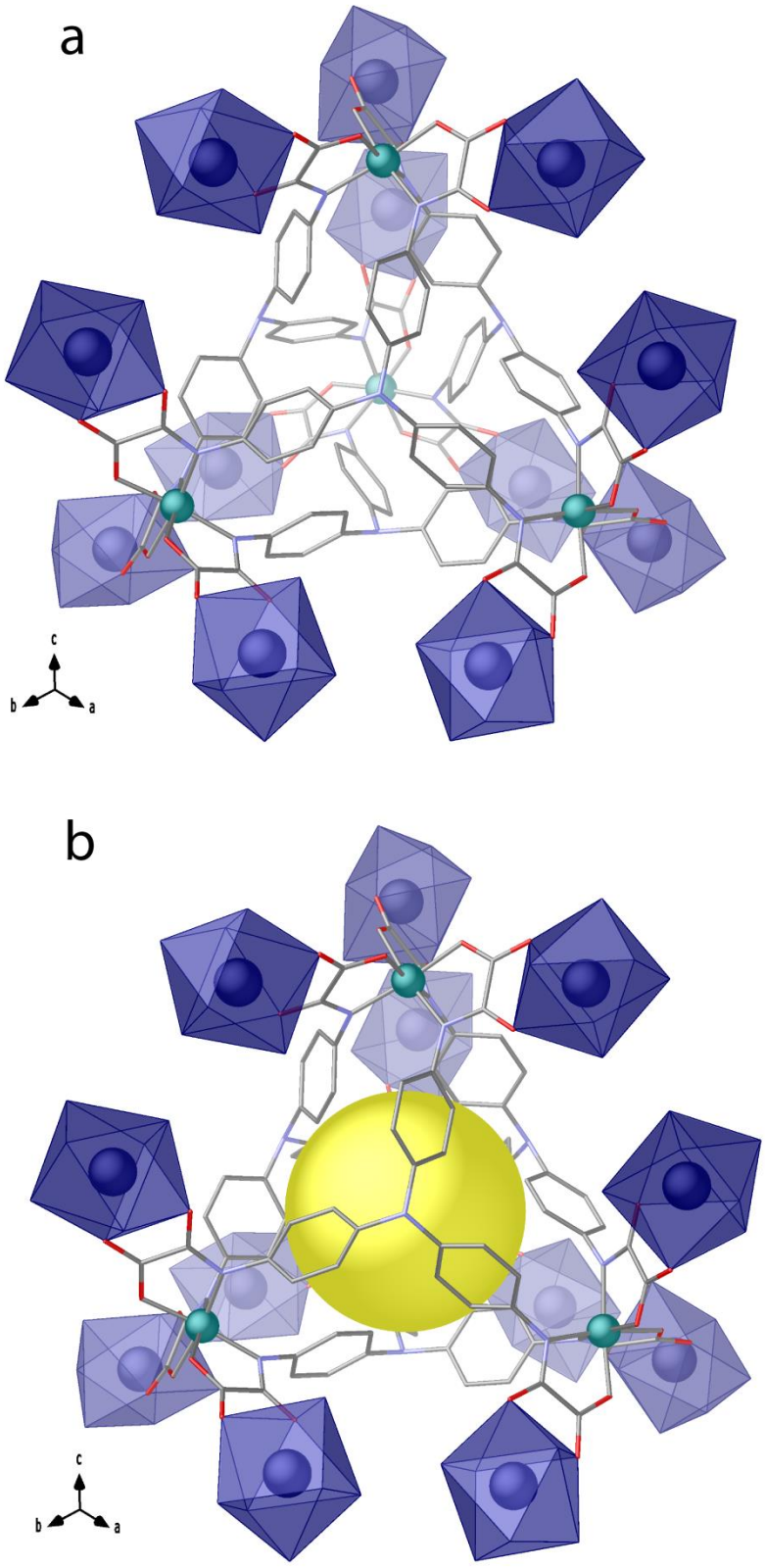

Figure S1. a) A portion of crystal structure of **1** along [111] direction showing [$Co_4(tpatox)_4$] tetrahedral cages of **1** connected by twelve Ca(II) metal ions residing in a bicapped trigonal prismatic geometry; in b) the cage's voids have been evidenced by yellow sphere. Ligands from the network are depicted as gray sticks, cobalt(III) and calcium(II) ions from the network are represented as cyan spheres and blue polyhedra, respectively.

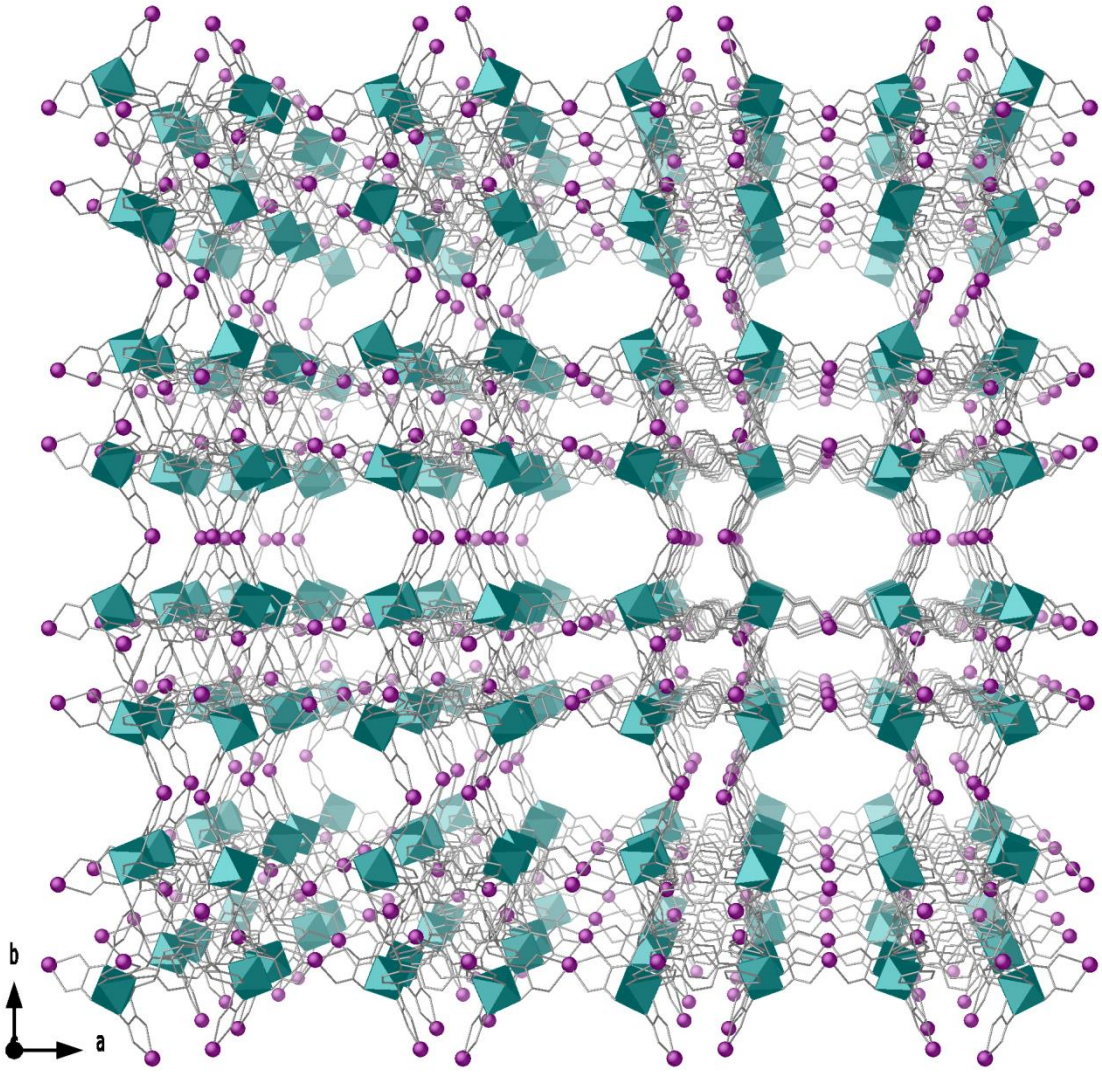

Figure S2. Perspective view along *c* crystallographic axis of porous structure of **3** (the detected crystallization water molecules are omitted for clarity). Ligands from the network are depicted as gray sticks, cobalt(III) and dysprosium(III) ions from the network are represented as cyan polyhedral and purple spheres, respectively.

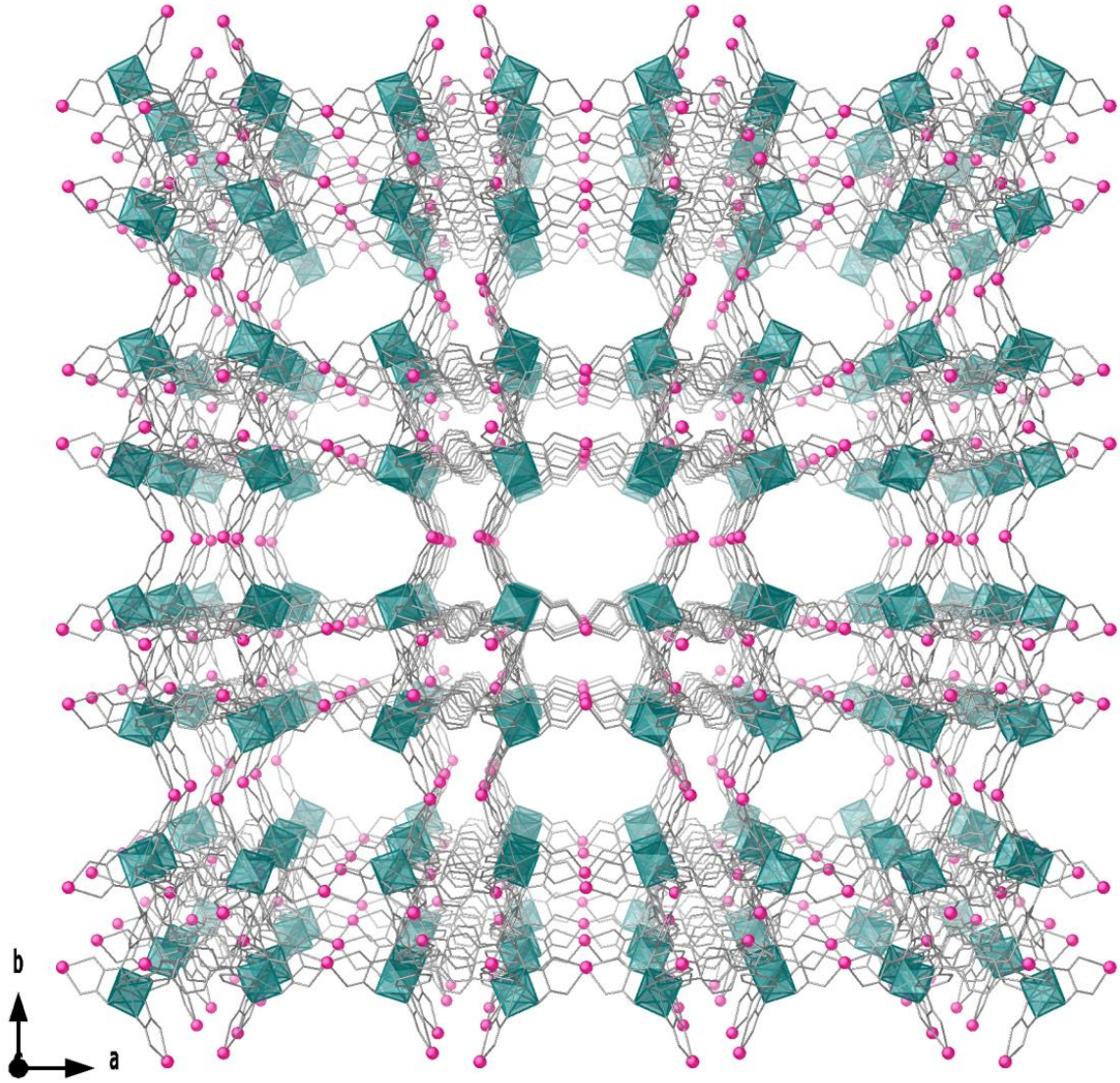

Figure S3. Perspective view along *c* crystallographic axis of porous structure of **4** (the detected crystallization water molecules are omitted for clarity). Ligands from the network are depicted as gray sticks, cobalt(III) and holmium(III) ions from the network are represented as cyan polyhedral and magenta spheres, respectively.

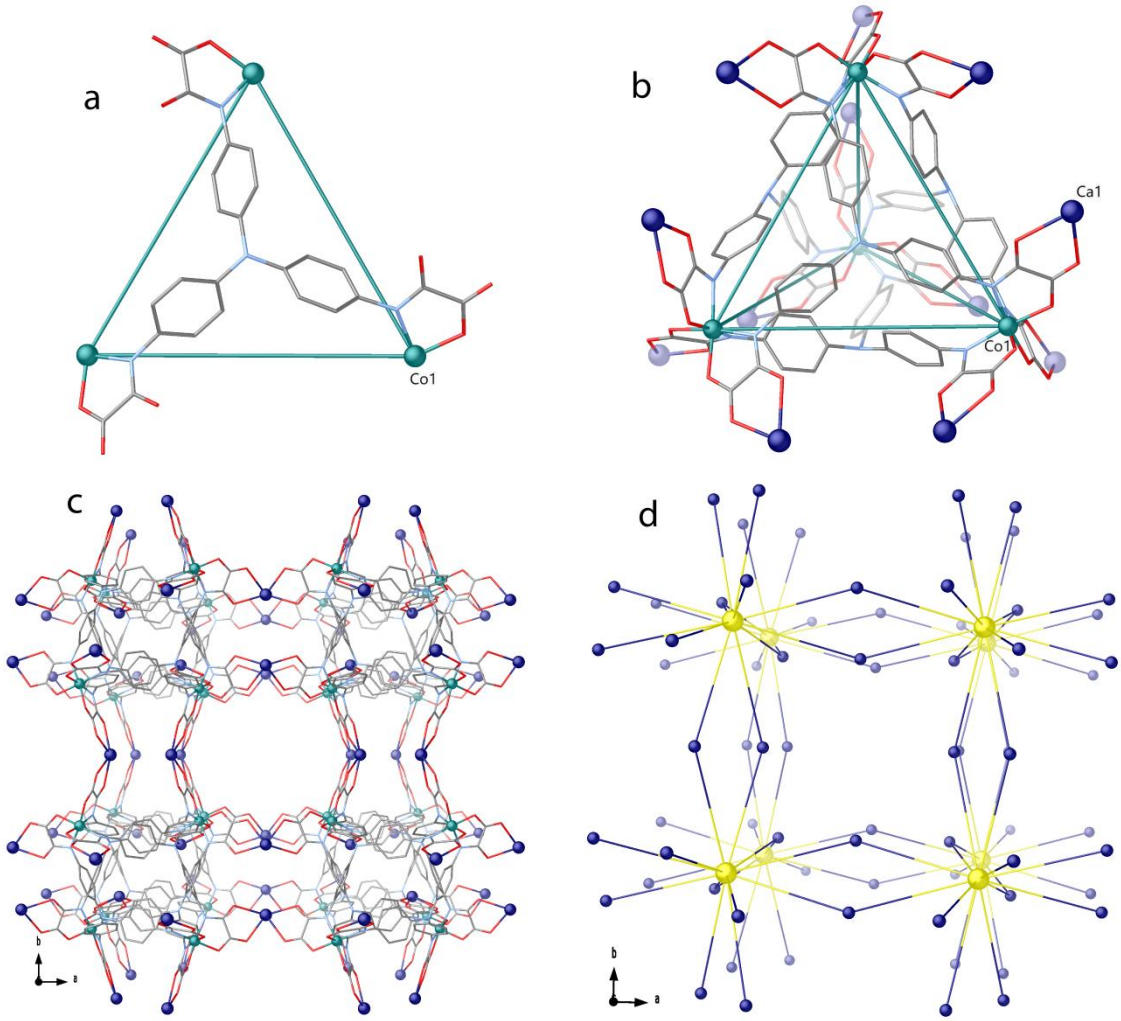

Figure S4. a) A fragment of crystal structure of **1** showing tripodal tpatox ligands as 3-connected nodes and b) $[Co_4(L)_4]$ tetrahedral cages with Co(III)···Co(III) separations underlined by cyan lines; c) Perspective view of a fragment of crystal structure showing eight cages connected by 2-c connected nodes; d) simplified underlying net obtained reducing tetrahedral cages as 12-connected nodes (depicted as yellow spheres). In a-c ligands from the network are depicted as gray sticks, cobalt(III) and calcium(II) ions from the network are represented as cyan and blue spheres, respectively.

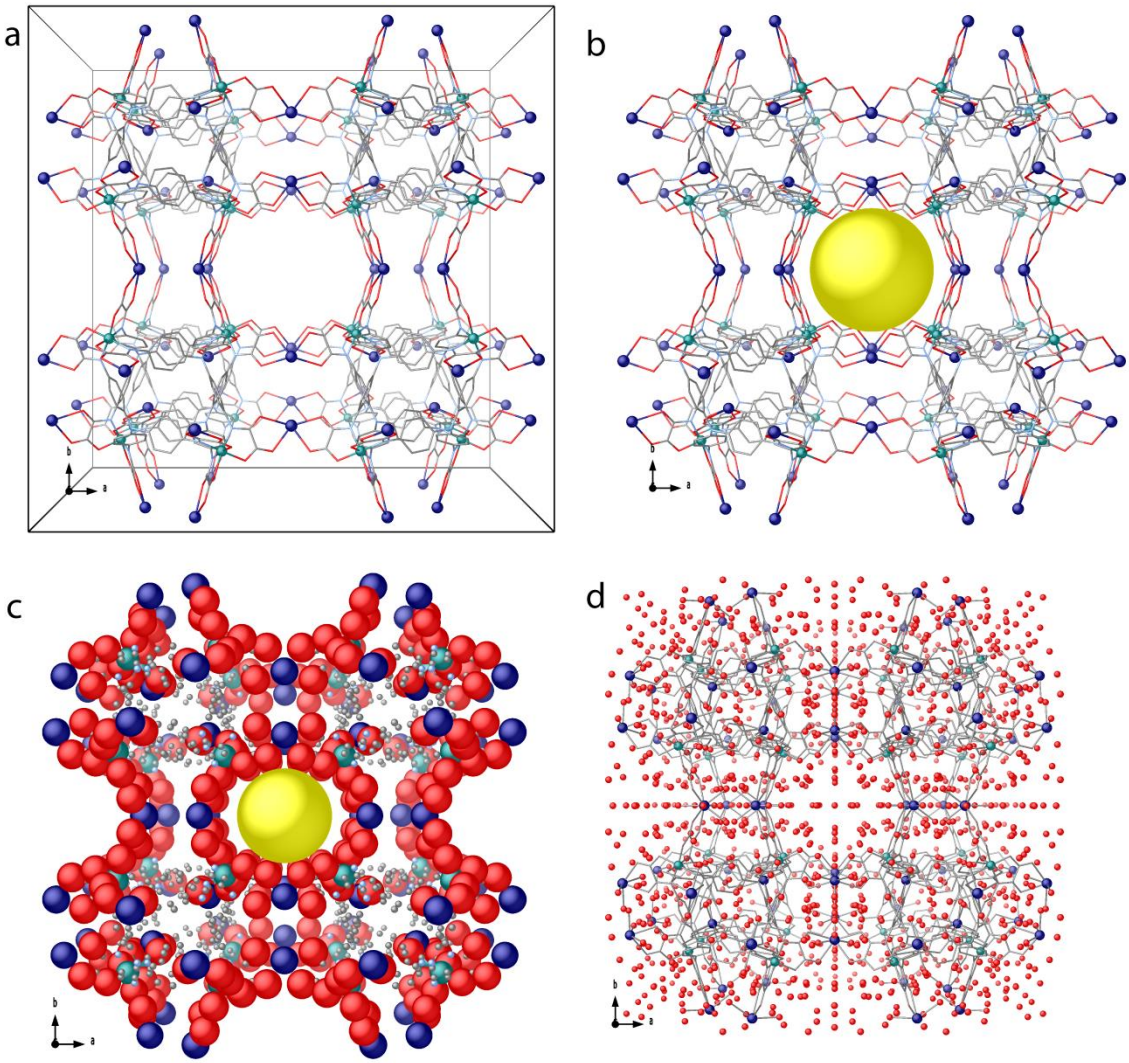

Figure S5. Perspective view of a fragment of crystal structure of **1** showing unit cell content (a); biggest pores underlined by yellow spheres in ball and sticks (b) and space filling (c) models; solvent accessible voids (close to 70% of the total volume) filled by solvent guests (red spheres) in **1** (d). Color code: calcium, blue, cobalt, cyan, carbon, grey, oxygen red, nitrogen sky blue.

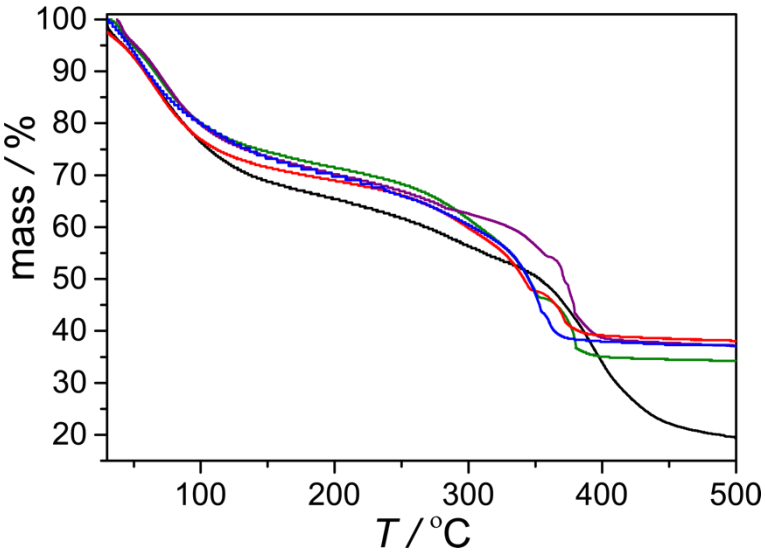

Figure S6. Thermo-Gravimetric analysis (TGA) of **1** (black), **2** (green), **3** (blue), **4** (purple) and **5** (red) under dry N_2 atmosphere.

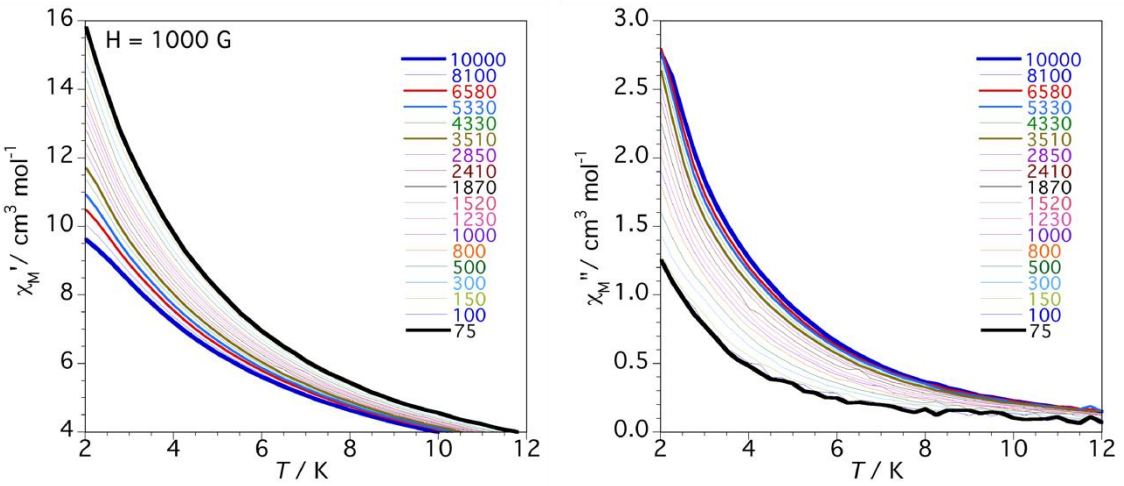

Figure S7. Temperature dependence of χ_M' (left) and χ_M'' (right) of **3** under an applied static field of 1000 G with a ±5.0 G oscillating field in the frequency range of 0.075–10 kHz (from black to green).

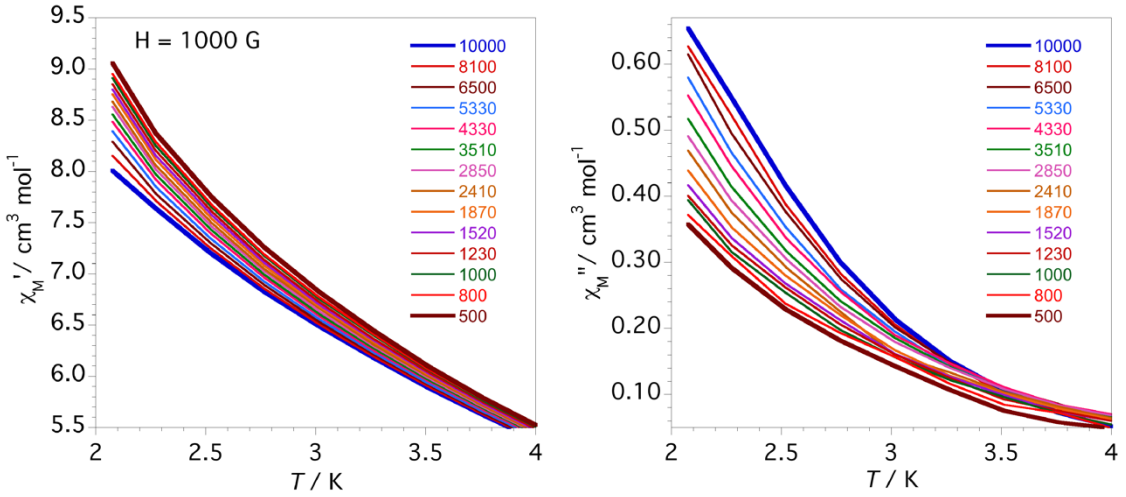

Figure S8. Temperature dependence of χ_M' (left) and χ_M'' (right) of **5** under an applied static field of 1000 G with a ±5.0 G oscillating field in the frequency range of 5–10 kHz (from black to green).

References

1. Gattuso, G.; Grasso, G.; Marino, N.; Notti, A.; Pappalardo, A.; Pappalardo, S.; Parisi, M. F. Amino Surface-Functionalized Tris(calix[4]arene) Dendrons with Rigid C_3-Symmetric Propeller Cores. *Eur. J. Org. Chem.* **2011**, 5696–5703.
2. SAINT, version 6.45, Bruker Analytical X-ray Systems, Madison, WI, 2003.
3. Sheldrick G.M. SADABS Program for Absorption Correction, version 2.10, Analytical X-ray Systems, Madison, WI, 2003.
4. (a) Sheldrick, G. M. Crystal structure refinement with SHELXL. *Acta Cryst. C* **2015**, *71*, 3–8. (b) Sheldrick, G. M. A short history of SHELX. *Acta Cryst. A* **2008**, *64*, 112–122. (c) SHELXTL-2013/4, Bruker Analytical X-ray Instruments, Madison, WI, 2013.
5. (a) Spek, A. L. *PLATON* SQUEEZE: a tool for the calculation of the disordered solvent contribution to the calculated structure factors. *Acta Crystallogr. Sect. C-Struct. Chem*. **2015**, *71*, 9–18. (b) Spek, A. L. Structure validation in chemical crystallography. *Acta Crystallogr. Sect. D, Biol. Crystallogr.* **2009**, *65*, 148–155.
6. Farrugia, L. J. *WinGX* suite for small-molecule single-crystal crystallography. *J. Appl. Crystallogr.* **1999**, *32*, 837–838.
7. D. Palmer, CRYSTAL MAKER, Cambridge University Technical Services, C. No Title, 1996.
8. PANalytical X'Pert HighScore Plus, **2012** PANaytical B. V., Almelo, The Netherlands.